

Applied Bionics and Biomechanics

Biomimicry and Bioinspiration as Tools for the Design of Innovative Materials and Systems

Lead Guest Editor: Saurabh Das

Guest Editors: Kollbe Ahn and Nadine Martinez





Biomimicry and Bioinspiration as Tools for the Design of Innovative Materials and Systems

Applied Bionics and Biomechanics

Biomimicry and Bioinspiration as Tools for the Design of Innovative Materials and Systems

Lead Guest Editor: Saurabh Das

Guest Editors: Kollbe Ahn and Nadine Martinez



Copyright © 2018 Hindawi. All rights reserved.

This is a special issue published in “Applied Bionics and Biomechanics.” All articles are open access articles distributed under the Creative Commons Attribution License, which permits unrestricted use, distribution, and reproduction in any medium, provided the original work is properly cited.

Editorial Board

Andrea Cereatti, Italy
Laurence Cheze, France
Christian Cipriani, Italy
Jose L. Contreras-Vidal, USA
Agnès Drochon, France
Fabio Esposito, Italy
Ángel Gil-Agudo, Spain
Eugenio Guglielmelli, Italy
Hiroaki Hobara, Japan
Serkan Inceoglu, USA

Zhongmin Jin, China
Kiros Karamanidis, Germany
Justin Keogh, Australia
Jan Harm Koolstra, Netherlands
Thibault Lemaire, France
Le Ping Li, Canada
Andrea Marinozzi, Italy
Craig P. McGowan, USA
Jose Merodio, Spain
Juan C. Moreno, Spain

Estefanía Peña, Spain
Simo Saarakkala, Finland
Fong-Chin Su, Taiwan
Wei Tan, USA
Amir A. Zadpoor, Netherlands
Stefano Zaffagnini, Italy
Li-Qun Zhang, USA
Nigel Zheng, USA

Contents

Biomimicry and Bioinspiration as Tools for the Design of Innovative Materials and Systems

Saurabh Das , B. Kollbe Ahn, and Nadine R. Martinez-Rodriguez
Editorial (1 page), Article ID 6103537, Volume 2018 (2018)

Research on Biomimetic Models and Nanomechanical Behaviour of Membranous Wings of Chinese Bee *Apis cerana cerana* Fabricius

Yanru Zhao , Dongsheng Wang, Jin Tong, Jiyu Sun, and Jin Zhang
Research Article (10 pages), Article ID 2014307, Volume 2018 (2018)

Innovative Design and Performance Evaluation of Bionic Imprinting Toothed Wheel

Zhihong Zhang , Xiaoyang Wang, Jin Tong, and Carr Stephen
Research Article (11 pages), Article ID 9806287, Volume 2018 (2018)

Crashworthiness Design for Bionic Bumper Structures Inspired by Cattail and Bamboo

Tao Xu, Nian Liu, Zhenglei Yu, Tianshuang Xu, and Meng Zou
Research Article (9 pages), Article ID 5894938, Volume 2017 (2018)

Study on Effects of Titanium Surface Microporous Coatings Containing Zinc on Osteoblast Adhesion and Its Antibacterial Activity

Quan-ming Zhao, Guang-zhong Li, Hao-ming Zhu, and Li Cheng
Research Article (4 pages), Article ID 2906575, Volume 2017 (2018)

Analysis of Drag Reduction Methods and Mechanisms of Turbulent

Gu Yunqing, Liu Tao, Mu Jiegang, Shi Zhengzan, and Zhou Peijian
Review Article (8 pages), Article ID 6858720, Volume 2017 (2018)

Editorial

Biomimicry and Bioinspiration as Tools for the Design of Innovative Materials and Systems

Saurabh Das ^{1,2,3}, **B. Kollbe Ahn**^{3,4} and **Nadine R. Martinez-Rodriguez**^{2,3,5}

¹Chemical Engineering, University of California, Santa Barbara, CA 93106, USA

²Materials Research Laboratory, Materials Research Science and Engineering Center, University of California, Santa Barbara, CA 93106, USA

³Marine Science Institute, University of California, Santa Barbara, CA 93106, USA

⁴Chemistry, University of Central Florida, Orlando, FL 94305, USA

⁵Stanford School of Medicine, Stanford, CA 94305, USA

Correspondence should be addressed to Saurabh Das; saurabh@engineering.ucsb.edu

Received 4 February 2018; Accepted 4 February 2018; Published 6 June 2018

Copyright © 2018 Saurabh Das et al. This is an open access article distributed under the Creative Commons Attribution License, which permits unrestricted use, distribution, and reproduction in any medium, provided the original work is properly cited.

Biological systems found in nature have inspired the study and design of engineering systems and modern technology. For instance, some species of geckos have a unique ability to quickly adhere to smooth vertical surfaces without the use of liquids or surface tension. The biomimetic gecko adhesive mechanism has influenced engineers to design and build adhesive platforms aimed at achieving robust and efficiently scaled adhesion for climbing on inverted surfaces with extreme topographical features. Similarly, sandcastle worms use a unique complex coacervate to glue together sand granules on the ocean floor whereas marine mussel adhesion is less specific and certainly more opportunistic than typical ligand-receptor interactions in protein adhesion. Adhesion in such marine organism is noteworthy due to its ability to overcome moisture and its ability to realize strong and reliable adhesion under water that most fabricated adhesives are lacking. Nature has developed surprisingly varied and, at times, rather ingenious lubrication strategies for controlling and regulating the interaction forces, friction, and wear at sheared interfaces; for example, the superlubricity and wear protection properties conferred by the complex synergy between the various proteins, polysaccharides, and lipids in the synovial fluid between articular joints in animals are rather startling. In this special issue, authors have discussed biomimicry techniques and ideas to engineer materials for imprinting technology, antibacterial surfaces, drag mitigating interfaces, impact-

resistant materials, and load bearing composites. Mathematical models have been used to explain the physics of the superior properties of the biomimetic materials. The practical use of the published research has been demonstrated by prototypes that mimic biological organisms.

*Saurabh Das
B. Kollbe Ahn
Nadine R. Martinez-Rodriguez*

Research Article

Research on Biomimetic Models and Nanomechanical Behaviour of Membranous Wings of Chinese Bee *Apis cerana cerana* Fabricius

Yanru Zhao ¹, Dongsheng Wang,¹ Jin Tong,² Jiyu Sun,² and Jin Zhang³

¹The College of Mechanical and Power Engineering, Henan Polytechnic University, Jiaozuo 454000, China

²The Key Laboratory of Bionic Engineering, Ministry of Education and the College of Biological and Agricultural Engineering, Jilin University, Nanling Campus, Changchun 130022, China

³United Automotive Electronic Systems Co. Ltd., Shanghai 200051, China

Correspondence should be addressed to Yanru Zhao; yanruzhao@163.com

Received 10 August 2017; Revised 30 October 2017; Accepted 5 December 2017; Published 19 February 2018

Academic Editor: Nadine Martinez

Copyright © 2018 Yanru Zhao et al. This is an open access article distributed under the Creative Commons Attribution License, which permits unrestricted use, distribution, and reproduction in any medium, provided the original work is properly cited.

The structures combining the veins and membranes of membranous wings of the Chinese bee *Apis cerana cerana* Fabricius into a whole have excellent load-resisting capacity. The membranous wings of Chinese bees were taken as research objects and the mechanical properties of a biomimetic model of membranous wings as targets. In order to understand and learn from the biosystem and then make technical innovation, the membranous wings of Chinese bees were simulated and analysed with reverse engineering and finite element method. The deformations and stress states of the finite element model of membranous wings were researched under the concentrated force, uniform load, and torque. It was found that the whole model deforms evenly and there are no unusual deformations arising. The displacements and deformations are small and transform uniformly. It was indicated that the veins and membranes combine well into a whole to transmit loads effectively, which illustrates the membranous wings of Chinese bees having excellent integral mechanical behaviour and structure stiffness. The realization of structure models of the membranous wings of Chinese bees and analysis of the relativity of structures and performances or functions will provide an inspiration for designing biomimetic thin-film materials with superior load-bearing capacity.

1. Introduction

Insects have developed their flight capacities of individual character during the long process of nature selection. The membranous wings of an insect are organs for flight behaviour, the weight of which is only 1-2% of its whole weight [1, 2]. The lifting force produced by insect membranous wings is about ten times higher than that of airfoil with the same area. Insects are magnificent in flight, and the flying behaviours include flapping flight, glide, hover, changing flying directions rapidly, and flight backward [3].

The research on biological membrane has attracted widespread attention due to insect membranous wings with specific structures and superior performances. The biological

membrane is a new field formed in the research of international high-tech materials in the 1990s. The research on biological membrane is very active in developed countries such as America, Japan, and Germany; moreover, it is of great importance in reforming traditional industries, for example, agriculture, building material, aviation, spaceflight, military industry, automobile, and cutting tool [4–6]. The biomimetic composite membrane has a very broad market prospect and important strategic significance, can be used on the airfoil of micro aerial vehicle and the bionic coating of military equipment, and can also be used as environmental protection material to replace harmful plastic products, for example, agricultural film [7]. The research on biological membrane has important meaning on bionics to biomimetic composite

membrane and has extensive application prospect on the fields of information technology, biotechnology, and new energy technology.

The research imitating insect membranous wings has been a hotspot at home and abroad. The model design imitating insect membranous wings has practical significance. The insect species is more and the forms of membranous wings are complicated and varied, which provides abundant natural sources for the research on biomimetic thin-film materials and biomimetic 2-dimensional composite materials [8, 9]. There are many factors affecting the model imitating insect membranous wings, such as the material property of veins and membranes, distribution and quantity of veins, and appearance of membranous wings [10–12]. The materials that are alike to insect membranous wings are less, so the appearance of membranous wings and distribution of veins are excellent reference for the biomimetic research before ideal materials can be found.

2. Materials and Methods

2.1. Sample Preparation and Test Equipment. Living Chinese bees, *Apis cerana cerana* Fabricius (Hymenoptera, Aculeata, Apoidea, Apidae), were gathered. The Chinese bees were anaesthetized, and then their membranous wings were cut off their bodies within 12 hours so that the in vivo structures can be reserved. The membranous wings were cleaned with distilled water and then were air-dried. The right forewings of Chinese bees were selected as research objects, because the right forewings with large areas are the main wings to bear loads in flight and have representativeness. The mass and morphological parameters of Chinese bees were measured by an electronic analytical balance (FA2004), a stereomicroscope (SZX12), and its image analysis system (OLYCIA™ M3). Figure 1 shows a stereoscopy photograph of the right forewing of the Chinese bee *Apis cerana cerana* Fabricius. Five Chinese bees were chosen randomly, and their morphological parameters were surveyed, and then the mean value was taken as the result. The mass $m = 94.38 \text{ mg} = 9.438 \times 10^{-5} \text{ kg}$. Length of the right forewing $a = 8.6 \text{ mm}$, and width of the right forewing $b = 2.8 \text{ mm}$. The area of the right forewing $A = 13.2 \text{ mm}^2$.

In order to avoid the influence of reflectivity, color, and curvature difference of the membranous wings on point cloud data collection, the dye penetrant imaging agent DPT-5 was used to deal with the membranous wings. Issues such as the fixing of the membranous wings, the spraying distance, and the uniformity of the coating should be paid attention to in spraying. Make sure that the coating is as thin and uniform as possible to diminish the effects of the spray to the results due to the membranous wings forming freeform surfaces [13–15].

A 3D laser-scanning system (LSV50) developed by 3D Family Technology Co. Ltd. was adopted. The surfaces of membranous wings of Chinese bees were scanned many times. The point cloud data were obtained by adjusting the scanning step and altering the measuring angle and position. The point cloud data are the base of the model



FIGURE 1: Stereoscopy photograph of the right forewing of a Chinese bee.

reconstruction, processing manufacturing, analog simulation, and feature analysis.

2.2. Setting Up of Structure Models of Membranous Wings of the Chinese Bee. The membranous wings of the Chinese bees dealt with DPT-5 were scanned by 3D laser-scanning system and were kept parallel to the scanning plane throughout the whole scanning process. The point cloud data were obtained, which inevitably introduces data error especially near sharp edges and the boundaries. The defective points of the point cloud data may cause the surface formed to deviate from the original surface; thus, the model reconstructed will be influenced. The jump points would come into being due to the change of calibration parameters of measuring equipment and the abrupt change of the measurement environment. The defective points and jump points have a great influence on the smoothness of curves in surface modeling. The sample holder and backing plate would also be scanned unavoidably in scanning, so first of all, the data unrelated to the research should be deleted during data processing.

The quality of point cloud data would become bad because of the interference by various noise. The point cloud data should be smoothed in order to eliminate or reduce the effects of noise, that is to say, let low-frequency data pass through and high-frequency noise are intercepted. The quality of a 3-dimensional model reestablished would be enhanced by data smoothing [16].

The information supplied by the parameters should remain constant, adopting a smoothing method. If the smoothness of data points of infinite nodes is considered, the offset function $\{P_n\}$ smoothed can be computed with linear superposition of the offset function $\{P_v\}$ as follows.

$$\{P_v\} \quad (v = \dots, -1, 0, 1, \dots),$$

$$P_n = \sum_{v=-\infty}^{+\infty} P_v L_{n-v}, \quad (1)$$

where $\{P_v\}$ is the offset function, $\{P_n\}$ is the offset function smoothed, and $\{L_v\}$ is the weighting factor and pair series, namely, $L_{-v} = L_v$.

The data $\{P_n\}$ is smoother than $\{P_v\}$; that is, the fluctuation of new data does not exceed that of the original data. The data disposed is not only smoother than before but also the deviation could not be too large.

Using reverse-engineering software, ImageWare, the point cloud data of the membranous wings of the Chinese



FIGURE 2: Structure model of the right forewing of a Chinese bee.

bees were smoothed with Gaussian filter. The weight in the specified domain of the Gaussian filter is Gaussian distribution. The average effect of the Gaussian filter is small, and the topography of the original data can be maintained well.

A large number of point cloud data would come into being when scanning the membranous wings of Chinese bees with the 3D laser-scanning system. High-density point cloud data contain massive redundant data. If the models are created with the point cloud data directly, a lot of time is needed to store and dispose the data and the whole process is uncontrollable. The point cloud data should be simplified before modeling.

The chord deviation sampling was used to reduce the point cloud data of the membranous wings of Chinese bees. The sampling of the scanning data is carried out by two parameters, the maximum deviation and maximum space in the chord deviation sampling. The maximum chord length was set, and points exceeding the extent would be deleted. The chord length between each point sampled and its adjacent points is within maximum deviation, and the space among points reserved is no more than the maximum space. In the chord deviation sampling, the characteristic points of surfaces reformed can be held well by identifying the curvature changes of data points so that the feature points and boundary points in the high curvature-variation region are persisted.

In reverse engineering, a common method for model reconstruction is to fit the point cloud data into spline curves with interpolation or approximation and the surfaces are accomplished with modeling tools such as sweep, blend, laying off curve, and four-side surface, and then the whole model can be gained by extension, clipping, and transition [17].

The models of Bezier, B-Spline, and NURBS have been used widely in CAD/CAM systems. For complex curves, Bezier and B-Spline are fit to deal with flat data, but NURBS can dispose of uneven data well [18–20]. The NURBS model was adopted to reconstruct the 3-dimensional geometric models of the membranous wings of Chinese bees.

The equation of NURBS curves can be shown as follows.

$$C(u) = \frac{\sum_{i=0}^n N_{i,p}(u) \omega_i P_i}{\sum_{i=0}^n N_{i,p}(u) \omega_i} = \sum_{i=0}^n R_{i,p}(u) P_i, \quad (2)$$

$$R_{i,p}(u) = \frac{N_{i,p}(u) \omega_i}{\sum_{j=0}^n N_{i,p}(u) \omega_j}, \quad (3)$$

where P_i is the control point; $N_{i,p}(u)$ is the B-Spline basis function of p order, ω_i is the weighted value, and u is the parameter value.

The 1-dimensional parameters are extended to 2-dimensional, and then the NURBS surfaces can be obtained, namely,

$$S(u, v) = \frac{\sum_{i=0}^m \sum_{j=0}^n N_{i,p}(u) N_{j,q}(v) \omega_{ij} P_{ij}}{\sum_{r=0}^m \sum_{k=0}^n N_{r,p}(u) N_{k,q}(v) \omega_{rk}} \quad (4)$$

$$= \sum_{i=0}^m \sum_{j=0}^n R_{i,p;j,q}(u, v) P_{ij},$$

$$R_{i,p;j,q}(u, v) = \frac{N_{i,p}(u) N_{j,q}(v) \omega_{ij}}{\sum_{r=0}^m \sum_{k=0}^n N_{r,p}(u) N_{k,q}(v) \omega_{rk}}, \quad (5)$$

where P_{ij} is the control point of the surface and $R_{i,p;j,q}(u, v)$ is the basis function of the NURBS surface.

According to the appearance characters of membranous wings of Chinese bees, the boundary curves were extracted from the point cloud data by the order Circle-Select Points, and then the 3-dimensional geometry model was rebuilt with the boundary curves and the rest of the point cloud data. The control points were added to the smoothed curves. The close degree to the real curves is good with more control points, and the curves would be smooth with less control points. Because the directions of curves are different and the distributions of control points are inhomogeneous, distortion, deformation, and reductus would come into being if the curves are used to form the surfaces directly. The boundary curves extracted should be close to the real boundaries of membranous wings of Chinese bees by means of adjusting the directions of curves, controlling the control points, adding or deleting nodes, smoothing curves, and reparametrization. The complete boundary curves were constructed by connecting the boundary curves adjusted together with the order Match 2 Curves. The model of the membranous wings of Chinese bees was accomplished with the boundary curves and the mixed point cloud data, as shown in Figure 2.

The morphological characters and main distribution of veins of membranous wings of Chinese bees were reproduced accurately by the structure model, which would provide a base for the setup of an exact finite element model.

2.3. Setup of Finite Element Model. The finite element software ANSYS does not specify a system unit for the analytical results. In structural analysis, any a self-contained unit system can be used according to the relevant parameters of different objects. A self-contained unit system is one in which the unit dimensions can be deduced from each other; that is, the data unit's input belongs to the same unit system in use [21]. All of the units relate to length and force, so other dimensions can be deduced from length, force, and time. Taking the smallness of membranous wings of Chinese bees into account, set length unit mm, force unit kN, mass unit kg, and time unit ms.

The veins of Chinese bees are hollow and their cross sections are approximately circular which were surveyed with a transmission electron microscopy (JEM-1200EX) made in Japan. The veins are formed of tracheas thickening, acting as the frame to sustain membranous wings, and the annular veins have better flexibility. The parameters of veins and

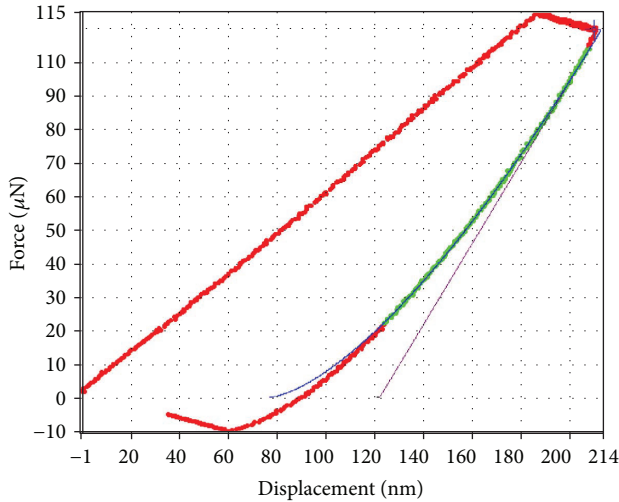


FIGURE 3: The force–displacement curve.

membranes were gained. The parameters of veins applied in finite element models were divided into two classes approximately: the external diameter of the first class veins is $R_1 = 130 \mu\text{m} = 0.13 \text{ mm}$ and the wall thickness $h_1 = 30 \mu\text{m} = 0.03 \text{ mm}$; the second class is $R_2 = 60 \mu\text{m} = 0.06 \text{ mm}$ and the wall thickness $h_2 = 15 \mu\text{m} = 0.015 \text{ mm}$. The thickness of membranes is $h = 1.5 \mu\text{m} = 0.0015 \text{ mm}$.

The material properties were obtained by a nanomechanical testing system, alias the nanoindenter (TriboIndenter) produced by Hysitron company, USA [22–25]. The maximum and minimum indenting forces used for tests were 30 mN and 100 nN, respectively; the load resolution is less than 1 nN and the step size of lengthway displacement is 13 nm. A Berkovich tip was used for determining the nanomechanical parameters of the wings. This kind of tip is often applied as a standard tip for nanoindentation tests.

A force–displacement curve can be obtained in real time and is shown in Figure 3 during the course of examining the nanomechanical parameters of the material with the nanoindenter. The nanohardness, the elastic modulus, the friction coefficient, the fracture stiffness, and the wear can be determined according to the force–displacement curve. The material properties include the elastic modulus of veins $E_1 = 1.12 \text{ GPa} = 1.12 \times 10^3 \text{ MPa} = 1.12 \times 10^3 \text{ N/mm}^2 = 1.12 \text{ kN/mm}^2$, the elastic modulus of membranes $E_2 = 1.5 \text{ GPa} = 1.5 \text{ kN/mm}^2$, and Poisson's ratio $\nu = 0.25$.

It is difficult to set up accurate 3-dimensional finite element models, because the cross-section corrugation is very small relative to the area of membranous wings of Chinese bees and the measuring accuracy of experimental instruments is very limited. The distributions and structure features of the veins and membranes of membranous wings of Chinese bees are researched emphatically, so establishing 2-dimensional finite element models are enough.

The structure model of membranous wings of Chinese bees made with ImageWare was imported into AutoCAD. The veins were drawn according to the geometric characteristics and distributions of veins of membranous wings of Chinese bees, as shown in Figure 4.

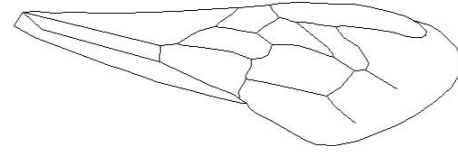


FIGURE 4: Vein distribution of the right forewing of a Chinese bee.

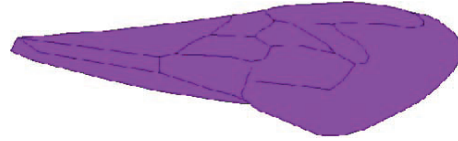


FIGURE 5: Finite element model of the right forewing of a Chinese bee.

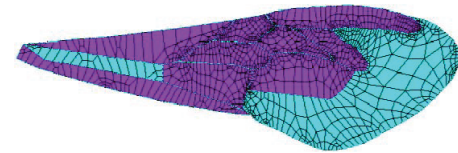


FIGURE 6: Finite element model meshed, and different colors show different element normals.

The veins of membranous wings of Chinese bees were turned into surfaces and then imported into ANSYS. The membranes were added on the model. Due to characteristic parameters of membranous wings of Chinese bees, the element type, material property, real constant, and element attribute of membranous wings were defined and the complete finite element model was produced, as shown in Figure 5.

The finite element model of membranous wings of Chinese bees was meshed. The finite element model can be divided into quadrilateral meshes or triangular meshes, and computational accuracy of quadrilateral meshes is higher than triangular meshes, so the quadrilateral meshes were adopted. The dimensions of meshes were set and local meshes refined. Figure 6 shows the finite element model meshed, and different colors show different element normals.

3. Results and Discussion

The flight mode of Chinese bees is flapping wing flight. The membranous wings of Chinese bees bear various loads in flight but fit well and fly steadily, and the damage or deformation is slight. Aiming at the flight characteristics of membranous wings of Chinese bees, several essential stress states were simplified. The deformations and stress states of the finite element model were researched under the concentrated force, uniform load, and torque.

3.1. Nanomechanical Behaviour under Concentrated Force.

The concentrated force was imposed on the finite element model of membranous wings of Chinese bees. The base of the finite element model was fixed, and the concentrated force was exerted on the rightmost node. The concentrated

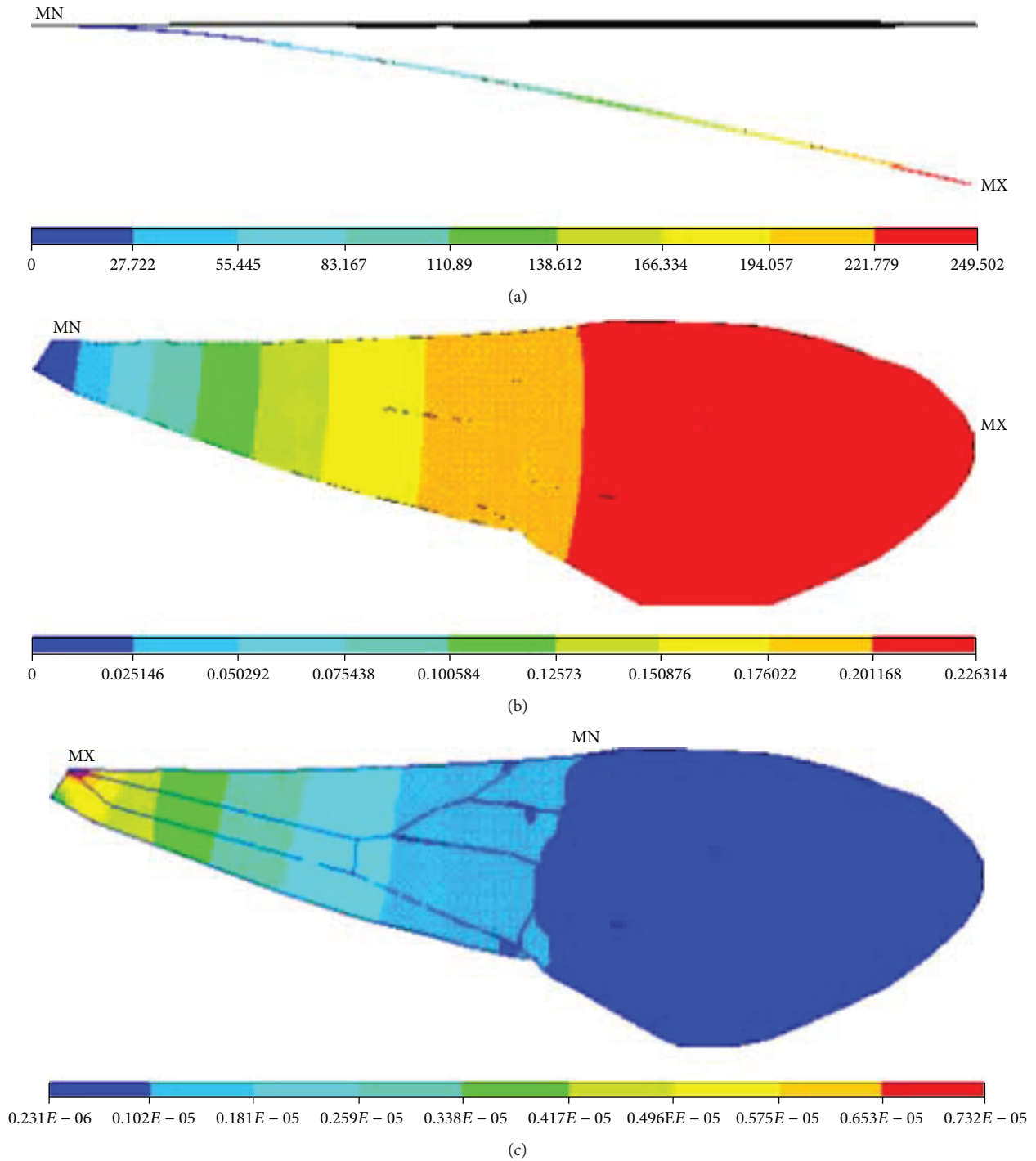


FIGURE 7: Nanomechanical behaviours of the finite element model of the right forewing of a Chinese bee under concentrated force: (a) displacements; (b) rotation angles; (c) stresses.

force is the ratio of gravity of the Chinese bee to areas of its all-membranous wings. The areas of forewings of the Chinese bee are larger than those of hindwings, and the ratio is about 3 to 2. The average mass of Chinese bees is about 94.38 mg measured by the electronic analytical balance above. The concentrated force born by the right forewing should be three tenths of the gravity of the Chinese bee, namely, 2.83×10^{-7} kN.

In order to observe clearly, the displacements of finite element models were magnified 200 times, and the rotation angles and stresses distributions remained unchanged. Figure 7 shows the nanomechanical behaviours of finite element models of membranous wings of Chinese bees under concentrated force. The deformations of finite element models increase from the basal part to the end gradually. The maximum structural deformations appear on the end

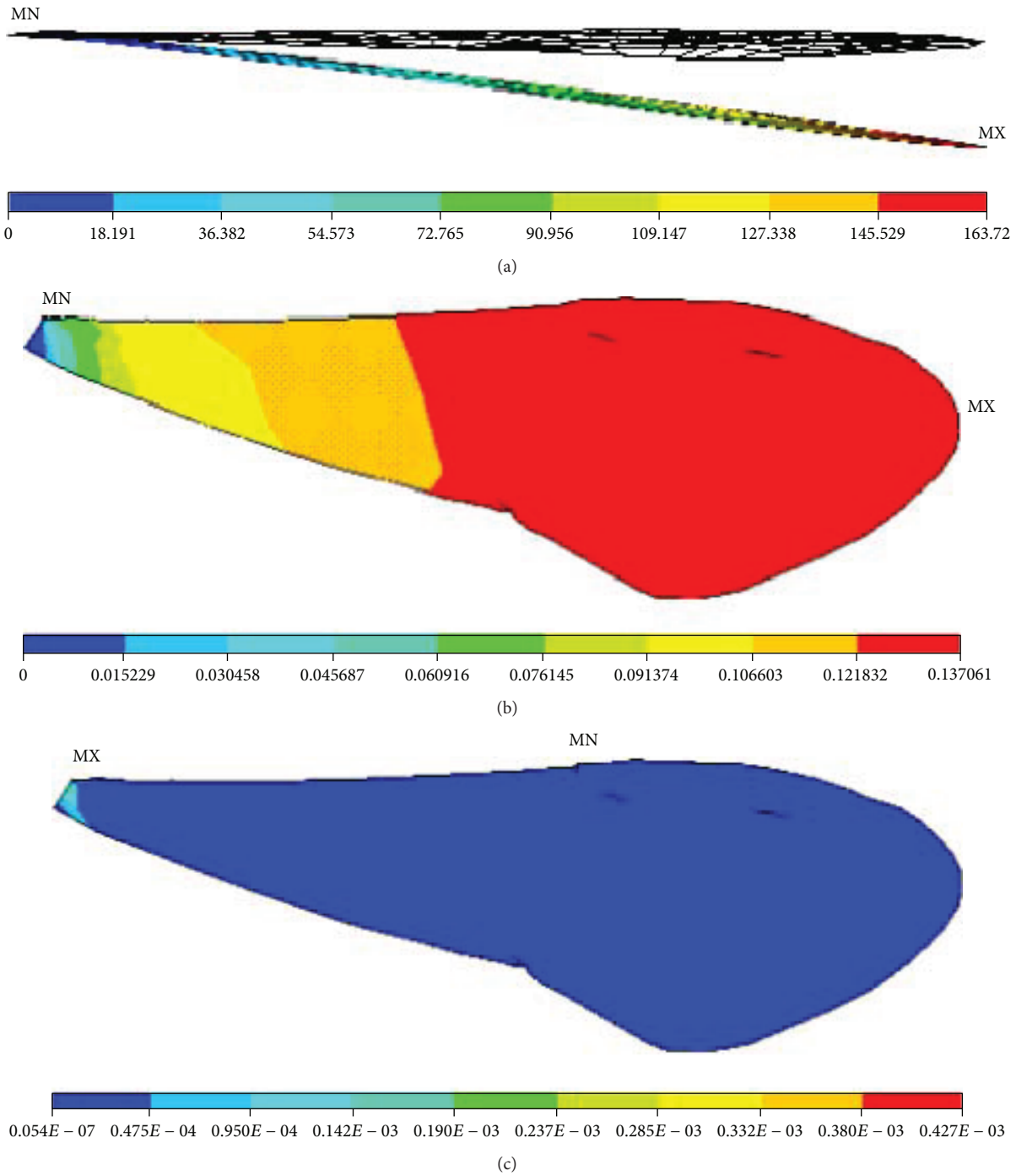


FIGURE 8: Nanomechanical behaviours of the finite element model of the right forewing of a Chinese bee under uniform load exerted on the anterior longitudinal vein: (a) displacements; (b) rotation angles; (c) stresses.

of the models. The maximal displacement is 1.25 mm and maximal rotation angle 0.226 rad, which illustrates the deformations of membranous wings of Chinese bees being large in flight. The large deformations are mainly because there are less veins and more membranes on the membranous wings of Chinese bees and the stiffness of membranes is far less than that of the veins. It is shown that the whole model deforms evenly, and the parts deforming abnormally do not appear.

It is indicated that the veins and membranes combine well into a whole to transmit loads effectively and the capacity of bearing load and resisting deformation of the membranous wings is increased. The stresses of finite element models decrease uniformly similar to displacements and rotation angles. The maximal stress appears on the top of the basal part and the minimal stress on the upper edge of the middle part.

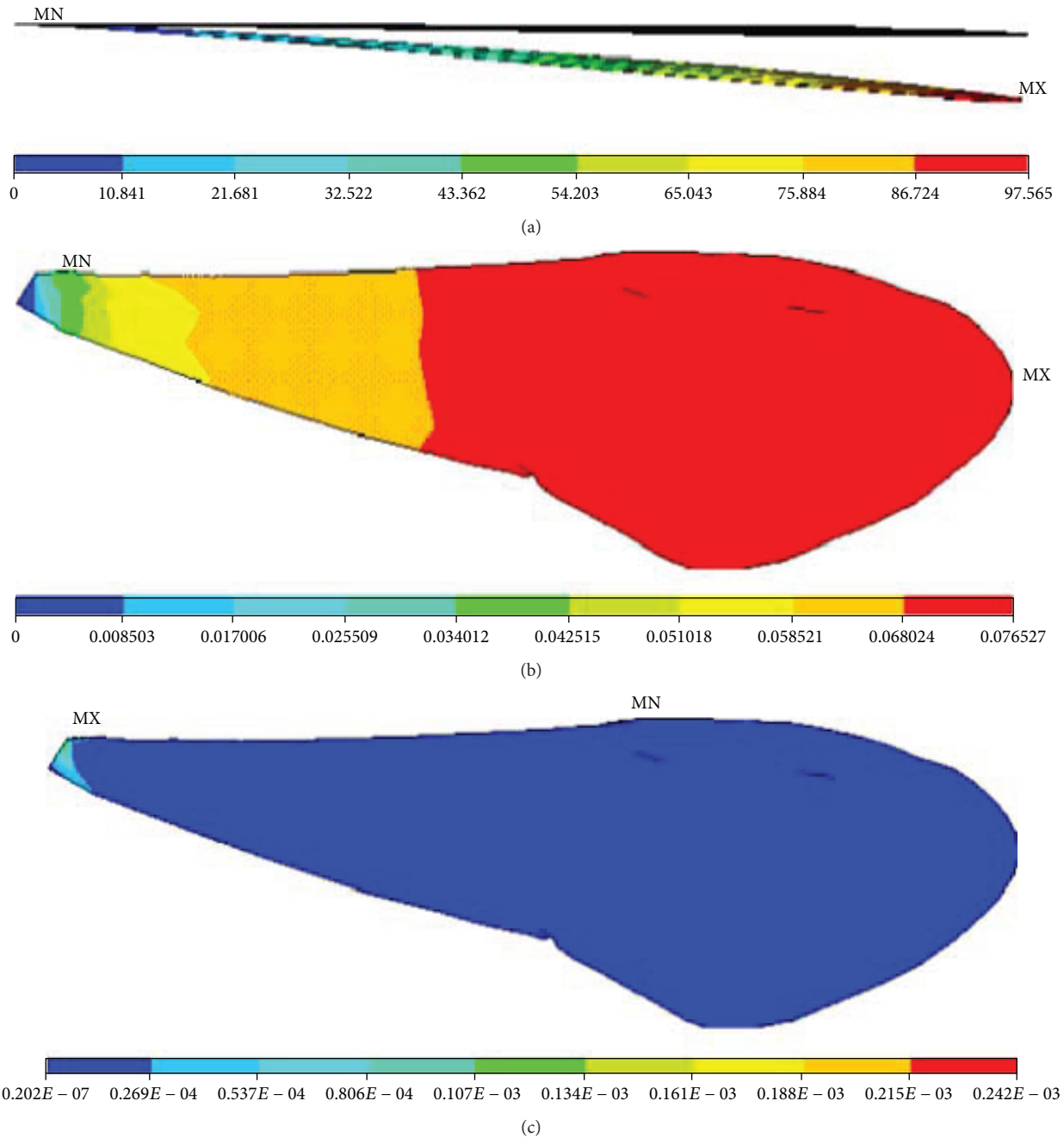


FIGURE 9: Nanomechanical behaviours of the finite element model of the right forewing of a Chinese bee under uniform load exerted on the whole membranous wings: (a) displacements; (b) rotation angles; (c) stresses.

3.2. Nanomechanical Behaviour under Uniform Load. The uniform load is one of the most important loads borne by insect membranous wings in flight. The uniform loads were exerted on the main veins and the whole membranous wings of Chinese bees, and the deformations and stress states of the finite element model were investigated.

The concentrated force borne by the right forewings of Chinese bees was scattered on the principal anterior longitudinal vein homogeneously. The uniform load is the ratio of concentrated force to the length of right forewing and is imposed on the finite element model vertically.

The concentrated force borne by the right forewing is 2.83×10^{-7} kN calculated above and the mean length of the right forewing is about 8.6 mm surveyed with the image analysis system above, so the uniform load is 3.3×10^{-8} GPa. Figure 8 shows the nanomechanical behaviours of finite element models of membranous wings of Chinese bees under uniform load exerted on the anterior longitudinal vein. It is illustrated that the changing trends of displacements and rotation angles under uniform load are similar to those under concentrated force but stress distributions are different obviously. The displacements are smaller than those under

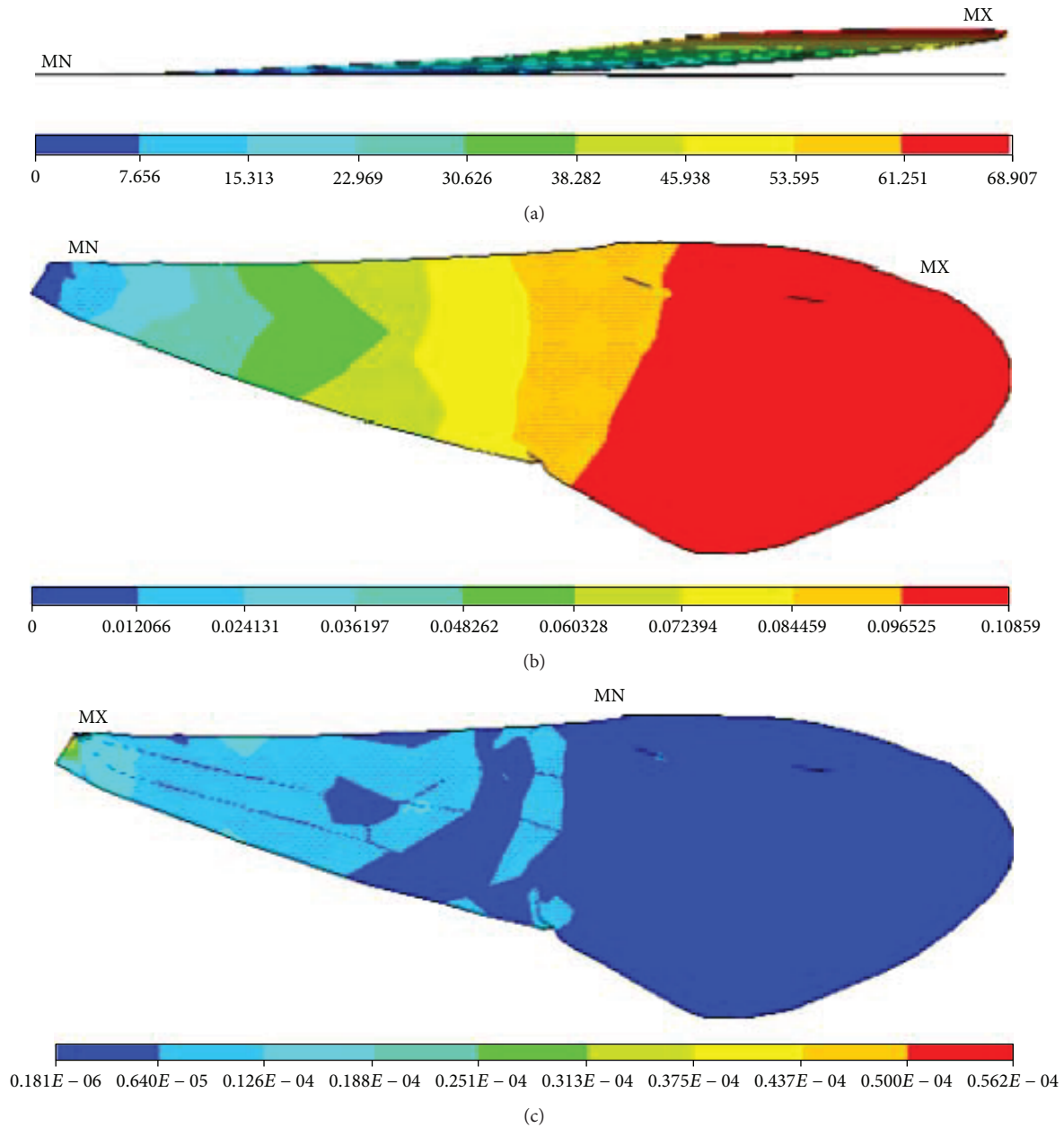


FIGURE 10: Nanomechanical behaviours of the finite element model of the right forewing of a Chinese bee under torque: (a) displacements; (b) rotation angles; (c) stresses.

concentrated force. Due to the uniform load exerted on the principal anterior longitudinal vein, the rotation angles on the upper edge of the finite element model are greater than those on the lower edge and the maximal rotation angle is smaller than that under concentrated force. The stresses are mainly focused on the basal part of the finite element model and small on the rest.

The uniform loads were imposed on the whole membranous wings of Chinese bees perpendicularly, and the magnitude is the ratio of concentrated force borne by the right forewing to its area. The average area of the right forewing is about 13.2 mm^2 tested with the image analysis system above, so the uniform load computed is 2.14×10^{-8} GPa. The restraint was exerted on the basal part of the finite

element model. Figure 9 shows the nanomechanical behaviours of finite element models of membranous wings of Chinese bees under uniform load exerted on the whole membranous wings. It is shown that the changing trends are alike to those under uniform load exerted on the anterior longitudinal vein, but the displacements and stresses are both reduced. The stresses are still mainly focused on the basal part of the finite element model and distribute on the whole membranous wings uniformly.

3.3. Nanomechanical Behaviour under Torque. A pair of loads whose magnitudes are equal and directions contrary was exerted on the leading edge and trailing edge of finite element models of membranous wings of Chinese bees

vertically. The magnitude is 2.14×10^{-8} GPa equal to the uniform load exerted on the whole membranous wings above. The displacement constraint was exerted on the basal part of the finite element model, the model was fixed, and then a pair of loads was imposed. Figure 10 shows the nanomechanical behaviours of finite element models of membranous wings of Chinese bees under torque. It is shown that only overall deformation of the model occurred under torque and the magnitude is far less than that under uniform load exerted on the whole membranous wings. It is illustrated that the model deviates upward from the initial position and the maximal displacement is 0.34 mm appearing on the end of the finite element model. Under the same loads, the large deformations are primarily due to only less and slender veins distributing on the trailing edge of membranous wings of Chinese bees. It is illustrated that rotation angles of finite element models increase from the basal part to the end little by little. On the same cross section, the deformations on middle parts are less than those on the leading edge and trailing edge, and the maximal rotation angle is 0.11 rad. There are no unusual deformations arising, and the deformations are small and transform uniformly, which once again testifies to the membranous wings of Chinese bees having fine global mechanical behaviour and structure stiffness.

It is indicated that the stress distributions of finite element models under torque are unlike those under concentrated force or uniform load. The greater stresses do not focus on the basal part of the finite element model totally and decrease from the basal part to the middle part gradually. The smaller stresses concentrate on the middle and posterior parts, and the maximal stress is 0.56×10^{-4} GPa arising on the basal part of the finite element model. On the same cross section, the stresses on the leading edge are larger than those on the trailing edge, which is due to the strong veins with great rigidity, and small deformation can bring large stresses under the same loads.

4. Conclusions

The surfaces of membranous wings of Chinese bees were scanned with a 3D laser-scanning system, and the systematic point cloud data were obtained. The defective points and data unrelated to research were deleted, and then the point cloud data were smoothed and simplified with reverse engineering. The 3-dimensional geometry model was rebuilt according to the appearance characters of membranous wings of Chinese bees. The deformations and stress states of the finite element model of membranous wings of Chinese bees were researched under the concentrated force, uniform load, and torque. The deformations of finite element models increase from the basal part to the end gradually and the maximum structural deformations appear on the end of models under concentrated force. The stresses decrease uniformly similar to displacements and rotation angles, and the maximal stress appears on the top of the basal part and minimal stress on the upper edge of the middle part. The displacements and stresses under uniform load exerted on the anterior longitudinal vein are smaller than those under concentrated force.

The stresses are mainly focused on the basal parts of models and small on the rest. The changing trends under uniform load exerted on the whole membranous wings are alike to those under uniform load exerted on the anterior longitudinal vein, but the displacements and stresses are both reduced. The large displacement appears on the end of models under torque. The rotation angles increase from the basal part to the end little by little, and on the same cross section, the deformations on the middle part are less than those on the leading edge and trailing edge. The greater stresses decrease from the basal part to the middle part gradually, and the smaller stresses concentrate on the middle and posterior parts. It is indicated that the veins and membranes combine well into a whole, and the deformations are small and transform uniformly, which illustrates the membranous wings of Chinese bees having excellent mechanical behaviour and structure stiffness.

Conflicts of Interest

The authors declare that there is no conflict of interest regarding the publication of this paper.

Acknowledgments

This work was supported by the National Natural Science Foundation of China (Grant no. 30600131, 50675087), by the Key Research Project in Colleges and Universities of Henan Province (Grant no. 17A460016), and by the Science and Technique Plan Project of Henan Technology Department (Grant no. 162102310431).

References

- [1] A. Ross, "Insect evolution: the origin of wings," *Current Biology*, vol. 27, no. 3, pp. R113–R115, 2017.
- [2] Y. Tomoyasu, T. Ohde, and C. Clark-Hachtel, "What serial homologs can tell us about the origin of insect wings," *F1000Research*, vol. 6, p. 268, 2017.
- [3] H. R. Hamdani, A. Aizaz, M. A. Naqvi, and National University of Sciences & Technology, "Force generation mechanisms by an insect wing in an idealized hovering motion," *Journal of Applied Fluid Mechanics*, vol. 10, no. 1, pp. 397–411, 2017.
- [4] H. Humburg, E. Volkmann, D. Koch, and J. Müssig, "Combination of biological mechanisms for a concept study of a fracture-tolerant bio-inspired ceramic composite material," *Journal of Materials Science*, vol. 49, no. 23, pp. 8040–8050, 2014.
- [5] K. Yu, G. Lan, B. Lu et al., "Evaluation of artificial skin made from silkworm cocoons," *Journal of Materials Science*, vol. 52, no. 9, pp. 5435–5448, 2017.
- [6] A. T. Dang and T. L. Kuhl, "Mind the line tension: new criteria for nanodomains in biological membranes," *Biophysical Journal*, vol. 112, no. 7, pp. 1291–1292, 2017.
- [7] G. Sun, Y. Fang, H. Zhi, and Z. Li, "Biomimetic fabrication of polymer film with high adhesive superhydrophobicity by duplicating locust wing surface," *Chemical Research in Chinese Universities*, vol. 31, no. 5, pp. 895–898, 2015.

- [8] J. Tong, Z. Chang, X. Yang et al., "Nanoindentation mechanical properties and structural biomimetic models of three species of insects wings," *Journal of Wuhan University of Technology-Mater. Sci. Ed.*, vol. 30, no. 4, pp. 831–839, 2015.
- [9] J. Prokop, M. Pecharová, A. Nel et al., "Paleozoic nymphal wing pads support dual model of insect wing origins," *Current Biology*, vol. 27, no. 2, pp. 263–269, 2007.
- [10] A. H. Faisal and A. Filippone, "Aerodynamic model for insect flapping wings with induced flow effect," *Journal of Aircraft*, vol. 53, no. 3, pp. 701–712, 2016.
- [11] S. J. McCauley, J. I. Hammond, D. N. Frances, and K. E. Mabry, "Effects of experimental warming on survival, phenology, and morphology of an aquatic insect (Odonata)," *Ecological Entomology*, vol. 40, no. 3, pp. 211–220, 2015.
- [12] Y. Zhao, J. Tong, and J. Sun, "Microstructure of the wings of dragonfly *Pantala flavescens* Fabricius and finite element analysis of its mechanical property," *Optoelectronics and Advanced Materials-Rapid Communications*, vol. 8, no. 7-8, pp. 794–799, 2014.
- [13] T. W. Lim, P. F. Ramos, and M. C. O'Dowd, "Edge detection using point cloud data for noncooperative pose estimation," *Journal of Spacecraft and Rockets*, vol. 54, no. 2, pp. 500–505, 2017.
- [14] M. Cheng, H. Zhang, C. Wang, and J. Li, "Extraction and classification of road markings using mobile laser scanning point clouds," *IEEE Journal of Selected Topics in Applied Earth Observations and Remote Sensing*, vol. 10, no. 3, pp. 1182–1196, 2017.
- [15] F. Bernard, L. Salamanca, J. Thunberg et al., "Shape-aware surface reconstruction from sparse 3D point-clouds," *Medical Image Analysis*, vol. 38, pp. 77–89, 2017.
- [16] D. Coeurjolly, M. Foare, P. Gueth, and J. O. Lachaud, "Piecewise smooth reconstruction of normal vector field on digital data," *Computer Graphics Forum*, vol. 35, no. 7, pp. 157–167, 2016.
- [17] H. K. Celik, A. E. Rennie, and I. Akinci, "Reverse engineering approach for precise measurement of the physical attributes related to the geometric features of agricultural products," *Journal of Food Measurement and Characterization*, vol. 11, no. 1, pp. 75–84, 2017.
- [18] L. Yu and X. Chendong, "Approximation of conic section by quartic Bézier curve with endpoints continuity condition," *Applied Mathematics-A Journal of Chinese Universities Series B*, vol. 32, no. 1, pp. 1–13, 2017.
- [19] R. C. Mittal and S. Dahiya, "A quintic B-spline based differential quadrature method for numerical solution of Kuramoto-Sivashinsky equation," *International Journal of Nonlinear Sciences and Numerical Simulation*, vol. 18, no. 2, pp. 103–114, 2017.
- [20] X. Liu, J. Peng, L. Si, and Z. Wang, "A novel approach for NURBS interpolation through the integration of acc-jerk-continuous-based control method and look-ahead algorithm," *International Journal of Advanced Manufacturing Technology*, vol. 88, no. 1-4, pp. 961–969, 2017.
- [21] Y. Zhao, D. Wang, J. Tong, J. Sun, and J. Zhang, "Statics analysis of dragonfly wing based on finite element model," *Transactions of the Chinese Society of Agricultural Engineering*, vol. 30, no. 15, pp. 33–38, 2014.
- [22] J. Tong, Y. Zhao, J. Sun, and D. Chen, "Nanomechanical properties of the stigma of dragonfly *Anax parthenope julius* Brauer," *Journal of Materials Science*, vol. 42, no. 8, pp. 2894–2898, 2007.
- [23] J. Sun, M. Ling, Y. Wang et al., "Quasi-static and dynamic nanoindentation of some selected biomaterials," *Journal of Bionic Engineering*, vol. 11, no. 1, pp. 144–150, 2014.
- [24] Y. Zhao, D. Wang, J. Tong, and J. Sun, "Nanomechanical behaviour of the membranous wings of dragonfly *Pantala flavescens* Fabricius," *Journal of Bionic Engineering*, vol. 13, no. 3, pp. 388–396, 2016.
- [25] D. Singh and B. Viswanath, "In situ nanomechanical behaviour of coexisting insulating and metallic domains in VO₂ microbeams," *Journal of Materials Science*, vol. 52, no. 10, pp. 5589–5599, 2017.

Research Article

Innovative Design and Performance Evaluation of Bionic Imprinting Toothed Wheel

Zhihong Zhang ^{1,2}, Xiaoyang Wang,¹ Jin Tong,^{3,4} and Carr Stephen⁵

¹Faculty of Modern Agricultural Engineering, Kunming University of Science and Technology, Kunming 650500, China

²United States Department of Agriculture, Agricultural Research Service, 1680 Madison Ave., Wooster, OH 44691, USA

³College of Biological and Agricultural Engineering, Jilin University, Changchun 130025, China

⁴The Key Laboratory of Bionic Engineering, Jilin University, Changchun 130025, China

⁵International Soil and Water Renewables, LLC, Salem, IN 47167, USA

Correspondence should be addressed to Zhihong Zhang; zzh_0822@hotmail.com

Received 11 August 2017; Accepted 18 October 2017; Published 8 January 2018

Academic Editor: Kollbe Ahn

Copyright © 2018 Zhihong Zhang et al. This is an open access article distributed under the Creative Commons Attribution License, which permits unrestricted use, distribution, and reproduction in any medium, provided the original work is properly cited.

A highly efficient soil-burrowing dung beetle possesses an intricate outer contour curve on its foreleg end-tooth. This study was carried out based on evidence that this special outer contour curve has the potential of reducing soil penetration resistance and could enhance soil-burrowing efficiency. A toothed wheel is a typical agricultural implement for soil imprinting, to increase its working efficiency; the approach of the bionic geometrical structure was utilized to optimize the innovative shape of imprinting toothed wheel. Characteristics in the dung beetle's foreleg end-tooth were extracted and studied by the edge detection technique. Then, this special outer contour curve was modeled by a nine-order polynomial function and used for the innovative design of imprinting the tooth's cutting edge. Both the conventional and bionic teeth were manufactured, and traction tests in a soil bin were conducted. Taking required draft force and volume of imprinted microbasin as the evaluating indexes, operating efficiency and quality of different toothed wheels were compared and investigated. Results indicate that compared with the conventional toothed wheel, a bionic toothed wheel possesses a better forward resistance reduction property against soil and, meanwhile, can enhance the quality of soil imprinting by increasing the volume of the created micro-basin.

1. Introduction

Arable farming land in semiarid environments is hampered by low and erratic rainfall. To use these lands effectively, techniques such as water harvesting (which may improve soil water storage and increase agricultural productivity) were developed [1–5]. “In situ” system is one of the simplest and cheapest rainwater harvesting approaches that has been practiced in many different farming systems. This technique involves the increase of the amount of water stored in the soil profile by trapping or holding the rainwater where it falls, then causing the captured water to sink rapidly into the root zone through the physics of soil and water hydrology. [6]. Soil imprinting is one approach of such “in situ” system

[7]; it is an operation whereby numerous geometrically ordered surface depressions are formed by modifying soil surface microtopography to collect and hold water in place during rainfall and allowing it to infiltrate the soil [8]. Consequently, water runoff is reduced, erosion is mitigated, and the water infiltration rate is increased. Hence, the approach of soil imprinting represents one of the most effective means of controlling both runoff and soil erosion [1–3, 9, 10]. As shown in Figure 1, the toothed wheel as a typical apparatus was used for soil imprinting, having a series of peripheral tooth circumscribing rolling wheel [11]. When this device is hauled and rolled across the soil surface, the soil flow around the tooth creates a lattice of consolidated discrete small depressions. Accordingly, the farming land was imprinted



FIGURE 1: Toothed wheel for soil imprinting on-farm field.

to the desired form to increase soil surface area in contact with water and is restructured, increasing the soil surface area by 30% on average. [5].

The efficiency of soil imprinting is measured by the quality of the imprinted microbasin, as well as the toothed wheel's forward resistance against soil. On the one hand, to ensure applicability, workability, and effectiveness of soil imprinting, depression shape and capacity should be adapted to ensure the satisfactory volume to achieve superior runoff collecting performance (Figure 2) [12]. On the other hand, as in any type of soil tillage operation, soil imprinting is energy consuming so effective energy-saving techniques for a toothed wheel design should be researched. Due to the rapid increase in fuel cost, the reduction of the energy consumption due to the tillage resistance is a necessity [13, 14].

Improving the shape design of a soil-engaging tool is one effective method for reducing operating resistance while increasing working quality [15]. The procedure of soil imprinting by a rotary toothed wheel involves soil shearing and compression at the tooth cutting edge; hence, the shape of the tooth can significantly affect the performance of soil penetrating and profiling of the microbasin, which in turn affects the quality of soil imprinting [16]. Therefore, a toothed wheel with different geometries should be introduced and attempts should be made to improve operating efficiency of soil imprinting.

For some 2.5 billion years on this planet, nature has been solving the problem of survival and has developed systems for success. It is an increasingly prosperous and promising approach to try to mimic nature's ways of meeting needs and solving problems. Historically, when pressed with an engineering problem, scientists and engineers would often fail to draw guidance and inspiration from the natural world [17]. The emerging science of "biomimicry" is offering new hope for solving old problems.

Soil-engaging tool designs based on geometrical structures of soil-burrowing animals were found to have the distinguished performance of low forward resistance against soil [18], and it was proved that the bionic designs imitating the geometrical features of the soil insect's digging limbs had remarkable effects on the performance of soil-engaging tools [19–22]. Hence, some characteristics of soil insects that have highly efficient soil-digging abilities have been carried out by researchers and have shown to successfully improve the working efficiency of soil-engaging components [23, 24].

A dung beetle (*Copris ochus* Motschulsky) is a special soil-burrowing animal, which can dig holes in hard and compacted soil at a high speed. The two forelegs of the dung beetle are fossorial ones with the special geometrical feature, offering a very stout-burrowing function to soil [25].

Through careful observation, it was found that when the dung beetle walks or burrows, the end-tooth of its foreleg interacts with soil continuously and directly. The end-tooth by which the dung beetle uses in cutting and digging of the soil has been improved and optimized through million years of evolution and adaptation, evolving a special outer contour curve structure. Therefore, a novel approach of the bionic geometrical structure was inspired for the design of an imprinting toothed wheel.

A bionically geometrical structure possesses enormous potential value for solving the problem of soil cutting and shearing resistance [26, 27]. Reverse engineering is a very useful tool for quantitatively revealing the biologically geometrical characteristics, which can bridge and transfer biological solutions to engineering techniques. The procedure of reverse engineering in bionics can be summarized as follows: an animal scan model was obtained, point clouds were gathered and processed, and CAD model and manufacture experimental prototype were reconstructed. Of all the steps in these procedures, quantitative analysis of the animal limb is the first step and groundwork. Effective reverse engineering operation can be realized if biological structure configurations were obtained efficiently and accurately. However, the difficulty is that the geometrical structure of a dung beetle's foreleg end-tooth is tiny and intricate. It is extremely difficult to survey and analyze the end-tooth outer margin's curve by traditional reverse engineering methods [19, 28]. Yet it was found that edge detection could be determined by a novel technique, which has been widely studied in recent years. Edge detection is a basic and important subject in computer vision and digital image processing [29], which can be used in segmentation, feature extraction, or identification of objects in a scene [30]. The essential process of edge detection is locating sharp discontinuities in an image, which originate from different scene features such as discontinuities in depth, discontinuities in surface orientation, and changes in material properties and variations in scene illumination [31]. Hence, based on previous studies [32], this edge detection technique was used to detect the outer edge of a dung beetle foreleg end-tooth capturing the two-dimensional point cloud of outer margin which is based on MATLAB software.

In this paper, geometric characteristics existing in a dung beetle's foreleg end-tooth was studied and its geometrical essence was abstracted. Based on a MATLAB software platform, edge detection in digital image processing technology was used to detect and capture the dung beetle's foreleg end-tooth outer margin two-dimensional point cloud. The outer margin two-dimensional point cloud was fitted by a nine-order polynomial function. Then, the special function curve was applied to the novel design cutting edge on a toothed wheel. Afterwards, the conventional and bionic imprinting toothed wheel was manufactured by means of a CNC machining center. Axles were mounted with both conventional tooth and bionic toothed wheels. The units were assembled, and traction tests in a soil bin were conducted. Taking required draft force and volume of imprinted depression as the investigating indexes, the working efficiency and quality of different toothed wheels were evaluated. Eventually, behavior and mechanism of different toothed wheels'

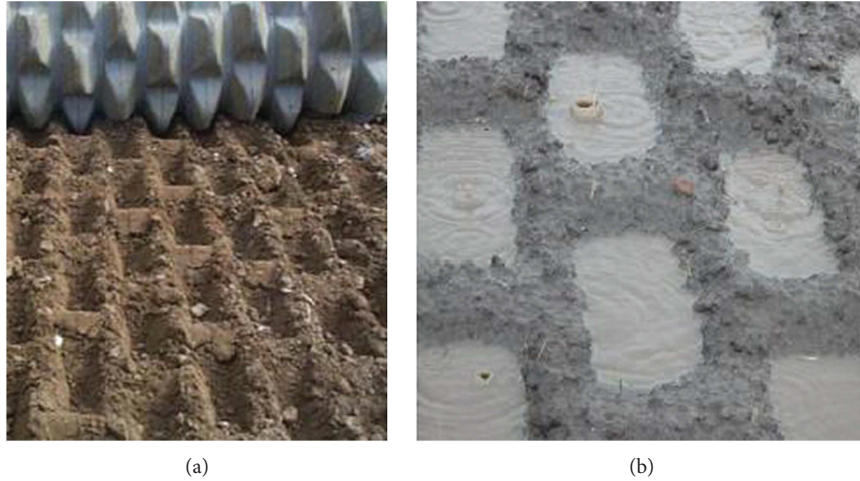


FIGURE 2: Imprinted soil surface for water harvesting. (a) Imprinted soil surface. (b) Microbasin for water harvesting.

interaction with soil were investigated by a finite element method.

2. Material and Methods

2.1. Sample Collection of Dung Beetle (*Copris ochus* Motschulsky). An adult dung beetle (*Copris ochus* Motschulsky) was captured in Changchun City, Jilin Province of China. The photograph of this species of dung beetle is shown in Figure 3. The sample was narcotized by 99% ether. Then, the forelegs as the selected components were separated from the body by scalpels, and the dung beetle was executed after the operation. Finally, the forelegs were washed with distilled water.

2.2. Morphological Image Processing. The geometrical morphology of the dung beetle (*Copris ochus* Motschulsky) was measured and observed with a stereoscope (STJ-30, Olympus Co. Ltd.). The end-tooth is in mesoscale, in which the height is about 1 mm and the width is about 0.5 mm. After irrelevant parts of the photograph were removed, it was sure that the end-tooth of the end-tooth to be analyzed is in the middle of the image. Figure 4 shows the original photograph input to the MATLAB program, and the size of the pixel was 669×727 .

2.3. Edge Detection and Obtaining of the Two-Dimensional Point Cloud. Mathematical morphology is a method applied in image processing. The basic idea is to measure and extract the corresponding shape from the image with structural elements for image processing and analyzing. Using mathematical morphology to detect the edge is better than using differential treatment, because it is not sensitive to noise, and the edge extracted is relatively smooth. The binary image is also known as the black-and-white image. The object can be easily identified from the image background. The combination of the binary image and mathematical morphology was adopted to detect an edge, which can reduce the noise and invalid edges and make the edge detection more smooth and

accurate. The MATLAB embedded functions “Rgb2gray,” “Imdilate,” “Imerode,” “Im2bw,” and “Imfill” were used to insure the extracted edge robust to noise and dulled edges. Eventually, the edge is detected by the “edge” function with the “LoG” operator. Figure 5 shows the flow-chart of this program.

2.4. End-Tooth Outer Margin Curve Fitting Model. After running the Matlab program, the X,Y coordinates of 809 points are taken by running the program. Figure 6 shows the two-dimensional point cloud of the end-tooth.

Nine-order polynomial function was chosen as the correct function for the accurate mathematical model in the process of curve fitting. The expression of the nine-order polynomial function is shown below:

$$f(x) = p_1 \times x^9 + p_2 \times x^8 + p_3 \times x^7 + p_4 \times x^6 + p_5 \times x^5 + p_6 \times x^4 + p_7 \times x^3 + p_8 \times x^2 + p_9 \times x + p_{10}. \quad (1)$$

In the equation above, $p_1 = 8.86 \times 10^{-20}$, $p_2 = -2.74 \times 10^{-16}$, $p_3 = 3.55 \times 10^{-13}$, $p_4 = -2.48 \times 10^{-10}$, $p_5 = 1.01 \times 10^{-07}$, $p_6 = -2.39 \times 10^{-05}$, $p_7 = 0.003032$, $p_8 = -0.1691$, $p_9 = 5.683$, and $p_{10} = -53.62$.

The correct definition of R^2 is 0.9982, which means this mathematical model can accurately represent the characteristics of end-tooth outer contour curves.

2.5. Manufacture of Toothed Wheel Prototype. For comparability of the volume of imprinted microbasin, both bionic and conventional teeth should be designed with similar dimensions. The volumes of conventional and bionic toothed wheels were 0.887 L and 0.881 L, respectively. The bionic tooth was only 0.68% smaller than the conventional tooth; this tiny volume difference is negligible when comparing the toothed wheel forward resistance and the volume of depression.

Ultrahigh molecular weight polyethylene (UHMWPE) boards of 80 mm thick were used to manufacture both conventional and bionic teeth. Based on the special outer contour curve-inspired form dung beetle foreleg end-tooth,



FIGURE 3: End-tooth on the foreleg of the dung beetle (*Copris ochus* Motschulsky).

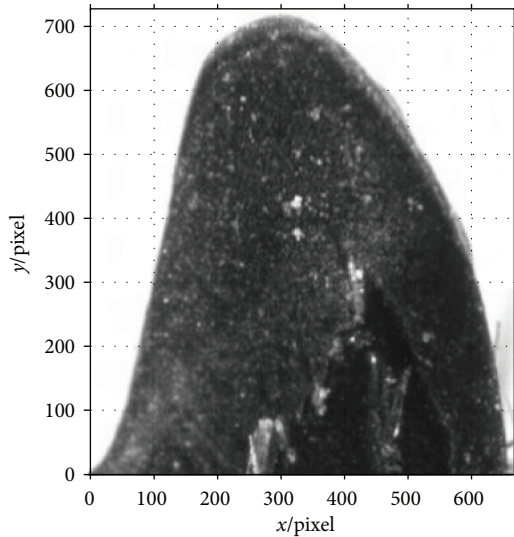


FIGURE 4: Original photograph of the end-tooth.

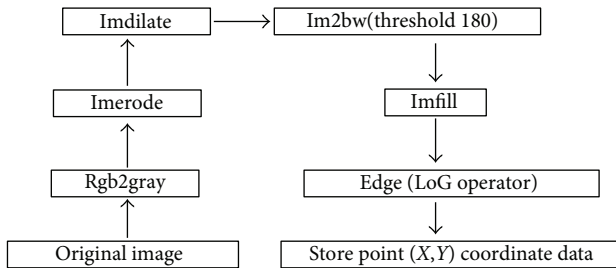


FIGURE 5: Program flow chart.

a bionic toothed wheel was designed, manufactured, and assembled on a steel cylindrical rolling wheel. Firstly, CNC milling machine was used to mill the arc surface of the tooth bottom that fits the cylindrical rolling wheel and then to process the tooth sides' bevel. Afterwards, the CNC machine center was used to cut the special outer contour curve on the edge of the bionic tooth. After that, a drilling machine was used to drill four screw holes. As shown in Figure 7, the conventional tooth had a straight cutting edge. The bionic tooth had a special outer contour curve on its cutting edge.

A total of 6-tooth units was fitted on a steel cylindrical rolling wheel with 320 mm diameter by a bolted connection and then was connected to a steel frame. Eventually, the

whole unit toothed wheel was trailed behind a soil bin carriage (Figure 8).

2.6. Soil Preparation. This study was conducted using the indoor soil bin facility at the Key Laboratory of Bionic Engineering (Ministry of Education, China), Jilin University. A soil bin (40 m long, 2.8 m wide, and 1.8 m deep) was used to produce a repeatable soil condition for the experiment, and a soil bin trolley was used to provide a constant forward travel speed. The yellow clay soil, which is typical soil of a large proportion of the maize and soybean growing regions of northeastern China, was used for this experiment. The soil preparation in each bin involved adding a predetermined amount of water to reach a targeted moisture content of 12.34% (w/w dry basis) with an average bulk density of 1200 kg/m³ (dry basis). The soil was covered with polyethylene sheets after watering to minimize moisture loss while allowing moisture to equalize within the bin. In the following day, loosening, mixing, and leveling to a set height were completed. Between runs of the experiment, a shovel was used to loosen the soil and a scraper blade was used to level the soil manually. Soil particle size distribution is listed in Table 1.

During the course of the tests, previously worked, the soil in the bin was covered with polyethylene sheets to avoid soil moisture evaporation from the air. Before conducting tests on the following day, soil samples were collected from the bin to monitor the bulk density and the moisture content.

2.7. Method of Data Collecting. The data sampling was conducted over 10 m long working section of the soil bin; 5 m long at each end of working section were buffering zones for trolley's deceleration and acceleration. A force sensor (LCS-S3) was set up between the toothed wheel and the front bar of the trolley carriage. Then, the force signal acquired by a force sensor was transferred to data acquisition system. Data acquisition system is shown in Figure 9, among which signal amplifier (RW-ST01A) was used to amplify force signal; then the amplified signal was transferred to a USB-powered portable measurement device (NI myDAQ, 200 kS/s, 16 bits, ± 10 V), and the measurement device was connected to a portable computer through a USB port. Eventually, force data were collected by an operation performed on a portable computer developed by LabVIEW software.

As shown in Figure 10, the experiments which measure the forward resistance of a toothed wheel were conducted using a trolley carriage. The trolley carriage moves on rail tracks on both sides of the soil bin. The toothed wheel

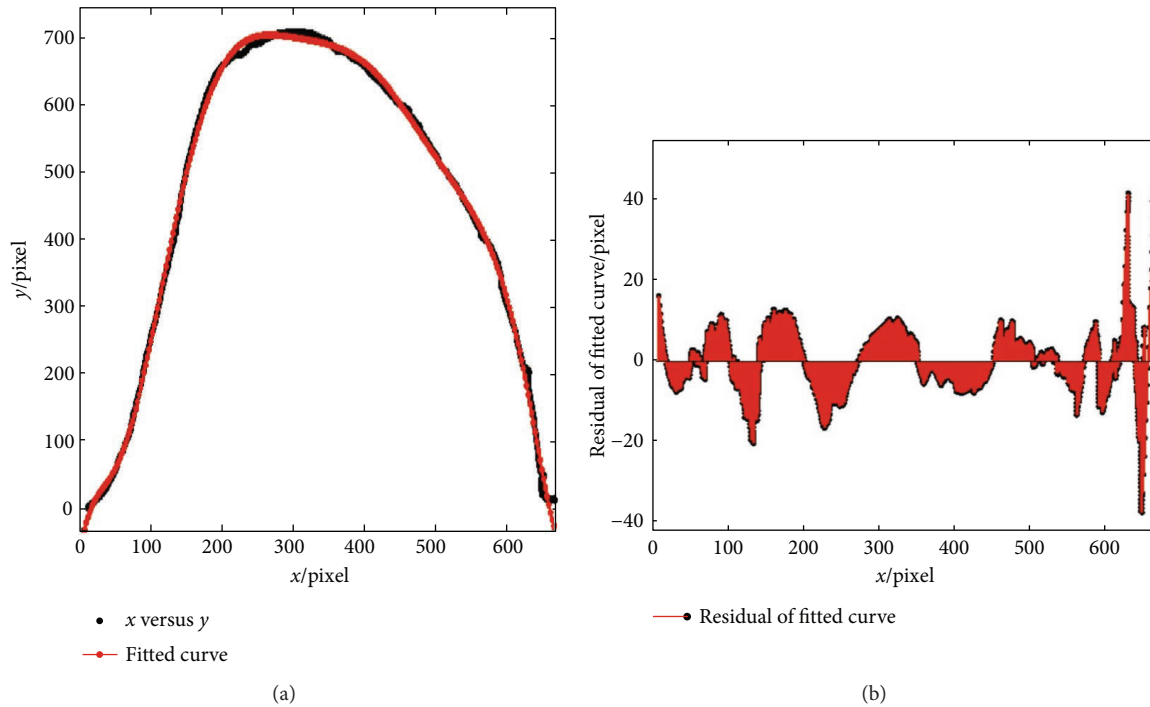


FIGURE 6: Extracted outer margin of the end-tooth. (a) Two-dimensional point cloud and fitted curve of the end-tooth. (b) Residual of the fitted curve.

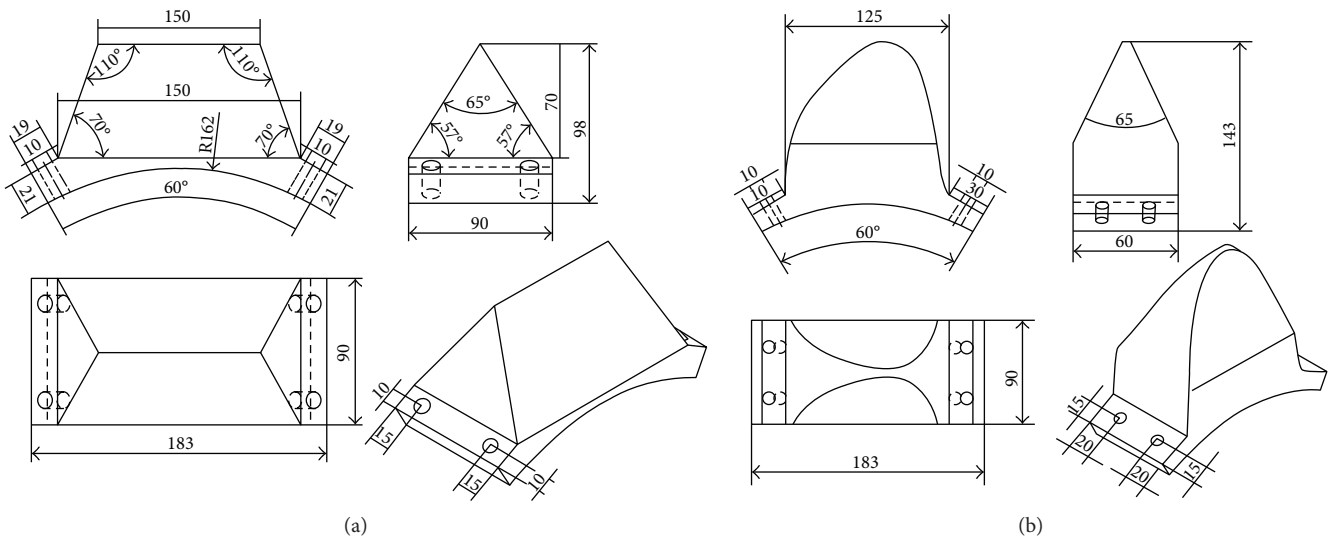


FIGURE 7: Scale drawing of different types tooth. (a) Conventional tooth. (b) Bionic tooth.

assembly was fitted to the test rig of trolley carriage which traveled at a forward speed of 1 m/s (typical speed of the toothed wheel for operating behind a four-wheeled tractor). Toothed wheels require adequate implemented load applied perpendicular to the soil surface, thus allowing the soil structure to be consolidated to create desired imprints. Implement weight was varied by the addition of ballast. The initial unladen weight of the toothed wheel was 250 N. To investigate effects of loads on a toothed wheel, weights were evenly

distributed on both sides of the rolling wheel shaft. The implement weights that were added on toothed wheels were 200, 250, 300, 350, and 400 N. At each load, a full replication of five experimental runs was completed over the soil bin. The collected data sets were statistically analyzed, and error bars were used to represent standard deviation.

2.8. Method of Evaluating Soil-Imprinting Quality. For any given soil conditions, the amount of water harvested by a



FIGURE 8: Manufactured axle mounted with wheels. (a) Conventional tooth. (b) Bionic tooth.

TABLE 1: The soil mechanical composition (sizes in mm).

Plastic limit W_p , %	Liquid limit W_L , %	Particle size distribution, %				
		0.1–0.05	0.05–0.01	0.01–0.005	0.005–0.002	<0.002
20.14	36.17	27	35	6.9	6.1	25

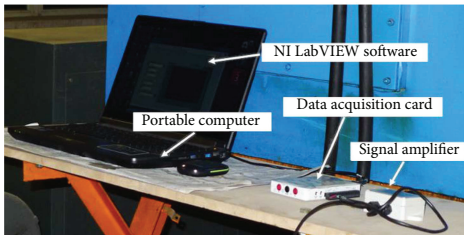


FIGURE 9: Data acquisition system.

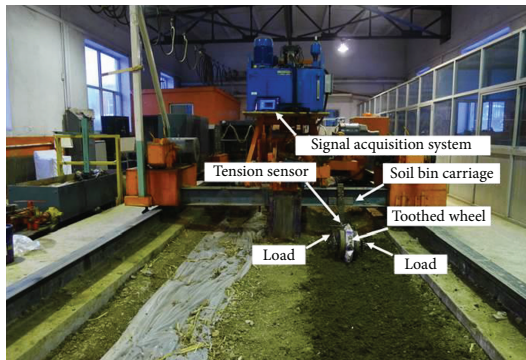


FIGURE 10: Forward resistance test platform for the toothed wheel.

depression depends on the depth of the depression and its volume; both of the indexes determine reservoir capacity and influence the working quality of soil imprinting. In order to evaluate reservoir capacity, a digital depth meter was used to measure the depth of each depression within 1 mm of accuracy. Meanwhile, the volume of each depression was determined by lining it with a thin plastic film (75 μm) and filling it with water to the surface, then the different readings from the measuring cylinder were calculated, and the volume of depression was determined (Figure 11). For each repetition, 20 depressions were selected randomly, the collected

data sets were statistically analyzed, and error bars were used to represent standard deviation.

2.9. Establish FEM Model for Investigating Interaction Mechanism between Soil and Toothed Wheel. To verify and compare the behavior of the soil and toothed wheel interface, stress results were achieved analytically by the FEM (finite element method) approach. Recent developments in computer technology have led to increasing applications of FEM to soil-tillage tool interactions [33]. FEM is very suitable at analyzing complex engineering problems, especially for dynamic systems with large deformation, and it has been used by many researchers to analyze problems related to soil mechanics [13, 34]. In this study, commercial finite code ABAQUS was used, a 3D finite element analysis of soil and toothed wheel interaction was carried out to investigate the behavior of the soil and toothed wheel interface. A calibrated finite element model [35] was established and provided realistic estimates of the stress at the contact interface between soil and toothed wheel, thereby predicting soil stress. As a compromise to cut down solution times, analyses were carried out through 1000 mm center movement in the horizontal plane along the x -axis direction within 1 s. Using an Intel i7-4790K, 4 GHz processor workstation PC with 24 GB of memory, full analysis jobs were created and submitted to the analyzer.

3. Results and Discussion

3.1. Effects of Bionic Outer Contour Curve on Toothed Wheel Forward Resistance. At each load, a full replication of five experimental runs was completed over the soil bin. The collected data sets of forwarding resistance were statistically analyzed, and error bars were used to represent standard deviation.

At the operating load of 200 N, 250 N, 300 N, 350 N, and 400 N, compare the forward working resistance of the



FIGURE 11: Methods for measuring the volume of depression.

toothed wheel mounted on different types of teeth. The results showed that the bionic toothed wheel reduced the forward resistance by 9.5%, 11.0%, 13.0%, 13.9%, and 16.5%, respectively, as compared with the conventional toothed wheel. The experimental data were analyzed by variance analysis. It was found the bionic toothed wheel can significantly reduce resistant force (p value < 0.01) as compared to the conventional tooth.

From Figure 12, it is noticeable that the forward resistance of the toothed wheel mounted with different types of teeth increases as the implemented load increases. When operating at small load, the difference of working resistance between the toothed wheel with the conventional tooth and that with the bionic tooth was less tangible. However, as the load increases, the working resistance of the bionic toothed wheel was obviously lower than those of the other types of teeth. It indicates that bionic toothed wheels require less draft force to operate; thus, energy consumption was reduced.

3.2. Effects of Bionic Outer Contour Curve on Imprinted Volume of Depression. For each repetition, 20 depressions were selected randomly. The collected data sets of depression volume were statistically analyzed, and error bars were used to represent standard deviation.

At the operating load of 200 N, 250 N, 300 N, 350 N, and 400 N, compare the volume of depression created by the toothed wheel mounted with the conventional and bionic tooth. Results showed that the bionic toothed wheel increased the volume of imprinted depression by 11.0%, 7.5%, 7.5%, 12.5%, and 24.9%, respectively, as compared with the conventional tooth. Experimental data were analyzed by analysis of variance. It was found the bionic toothed wheel can significantly increase the volume of depression (p value < 0.05) as compared to the conventional toothed wheel.

From Figure 13, it is noticeable that the volume of depression created by the toothed wheel mounted with both types of tooth increases as the implemented load increases. When operating at a small load, the working resistance between both toothed wheels the conventional tooth and bionic tooth showed the subtle difference. But as the operating load increases, the difference becomes increasingly remarkable.

3.3. Investigating Mechanism of Bionic Toothed Wheel Working Efficiency by Finite Element Method. For the finite element method (FEM) model of interaction between soil and conventional toothed wheel, solution time was about 96 h. Due to the relative complexity of the geometry of this

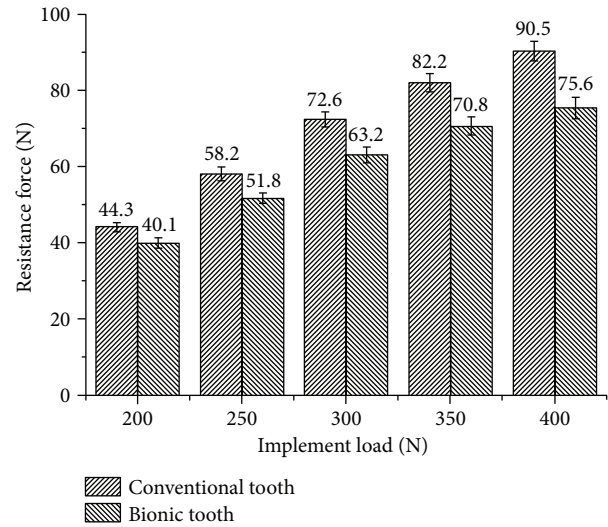


FIGURE 12: The test result of forwarding resistance for conventional and bionic toothed wheel.

bionic toothed wheel, the FEM model solution time reached 112 h. Both of the analyses were accomplished satisfactorily without element distortion or interruption.

As shown in Figures 14–16, soil stresses on toothed wheel and soil interface were predicted; contours on the deformed shape were plotted. The evolution of the S. Mises stress spectrum field for the bionic toothed wheel and conventional toothed wheel that was rolled over soil surface was outputted. The interaction between soil and the toothed wheel is a continuous process, yet in this study, 3 separate working phase stages were defined based on toothed wheel working characteristics: Figure 14 shows the impact stage (0.988 s), Figure 15 shows the penetrating stage (1.118 s), and Figure 16 shows the lifting stage (1.248 s).

A stress concentration (also called stress raisers) is a location in an object where stress is concentrated. Examples of shapes that cause these concentrations are cracks, sharp corners, holes, and changes in the cross-sectional area of the object. Stress concentration phenomenon can be observed when investigating the mechanism of toothed wheel interaction with soil by the finite element method. The soil material is strongest when force is evenly distributed over its area; however, geometric discontinuities cause soil material to experience a local increase in the intensity of a stress field. Therefore, soil material ceases to function satisfactorily because they break before either excessive elastic deflection or general yielding occurs [36, 37]. The special curvature of the contour curve on a bionic toothed wheel can cause geometric discontinuities in the soil; these discontinuities induced sudden increases in the stress (stress peaks) at points near the stress raisers, thus resulting in a localized increase in stress. Such stress concentrates within the soil causing it to fail more easily.

Hence, bionic outer contour edge with special curvature has the ability to maximize stress concentrations in soil, thus increasing the tendency of the soil material to fail. In other words, nonuniformity of stress may occur

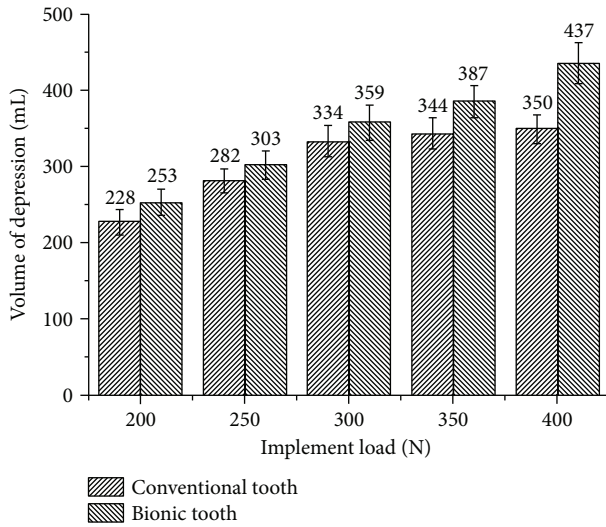


FIGURE 13: Test result volume of depression created by conventional and bionic toothed wheel.

because of geometric changes. Changes occur such as curvature variation in toothed wheel cutting edge. This non-uniformity in stress distribution may result in a maximum stress in a section that is considerably larger than the average stress. The term “stress gradient” is used to indicate the rate of increase of stress as a stress raiser is approached. Such stress gradient may have an influence on the damaging effect of the peak value of the stress. At the impacting and penetrating stages, as shown in the stress spectrum field from Figures 14–15, on the soil and toothed wheel interaction surface, the calculated stress gradient of the bionic tooth is steeper in the region of stress concentration than conventional tooth, so stress caused by the special outer contour curve of the bionic tooth showed more abrupt changes in section as compared to conventional tooth. Therefore, soil compaction fails more easily under the bionic tooth than the conventional tooth.

The level of concentrated stress can be evaluated by a stress concentration factor, which is the ratio of the highest stress to a referenced stress. In this study, the same load was applied to the toothed wheel sharing similar weight; hence, reference stress in soil caused by different toothed wheels was similar. By comparing the highest stress in soil and toothed wheel interfaces, stress concentration factors can be evaluated indirectly by using the highest stress value which was obtained in ABAQUS at the impacting stage and penetrating stage. At both of the stages, it is preferable to cause concentrated stress in the soil, as soil material fails more easily, thus increasing the volume of depression and reducing the required draft force. As compared to the bionic tooth, the maximum S. Mises stress value of the bionic tooth increased from 38.6 kPa and 46.2 kPa to 44.0 kPa and 52.9 kPa. The increment ratio was 14.1% and 14.4%, respectively. However, it is worth noting at the lifting stage that the conventional toothed wheel needs to uplift from the microbasin smoothly; it is desirable to cause less stress in the soil to protect the microbasin sides from collapsing. As

compared to the bionic tooth, the maximum S. Mises stress value of the bionic tooth reduced from 37.9 kPa to 33.4 kPa. The decrement ratio was –11.8%. Hence, the quality of soil imprinting was enhanced and forward resistance was reduced via the bionic design wheel.

When the toothed wheel impacts and penetrates the soil, the maximum value of stress is on the element near the bionic tooth cutting edge where the stress concentration occurs. A focus point of stress in soil is very likely to be its point of failure. As shown in Figure 17, soil under the bionic tooth was subjected to more stress concentration; thus it is unable to resist the highly concentrated stress and hence fails more quickly. But, when the bionic toothed wheel was lifted from the soil, stress was evenly distributed on soil and toothed wheel interface; thus bionic toothed wheel was easier to be lifted from the soil. Eventually, the forward resistance of the bionic toothed wheel can be reduced and soil imprinting quality can be enhanced.

4. Conclusion

Based on the observation that the highly efficient soil-burrowing dung beetle (*Copris ochus* Motschulsky) has intricate outer contour curves on its foreleg, this special outer contour curve was applied to the bionic design of imprinting toothed wheel to reduce its forward resistance and increase the working quality of soil imprinting simultaneously. The effect of the conventional and bionic toothed wheel at 5 vertical implemented loads (200 N, 250 N, 300 N, 350 N, and 400 N) on the forward resistance and depression parameters that were used for soil imprinting was investigated. This study recommends the use of this novel designed bionic tooth for soil imprinting. This recommendation is based on the following evidence:

- (1) Taking forward resistance as an index of evaluation, when the toothed wheel was mounted on both types of teeth operating at different implement loads, the forward resistance increased with the implemented load. The bionic toothed wheel can significantly reduce resistant force (p value < 0.01) as compared to conventional teeth. As the operating implemented load increases, the forward resistance reduction of the bionic tooth becomes increasingly obvious.
- (2) Using the volume of depression as an index of inspection, results showed that the volume of depression increased with the implemented load. Meanwhile, the bionic toothed wheel can significantly increase the volume of imprinted depression (p value < 0.05) as compared to the conventional toothed wheel. In addition, the reduction effects tend to be more obvious as the implement load increases.
- (3) Compared with the conventional toothed wheel, the bionic toothed wheel can reduce required draft force up to 16.5% and expand the volume of imprinted microbasin up to 24.9%.

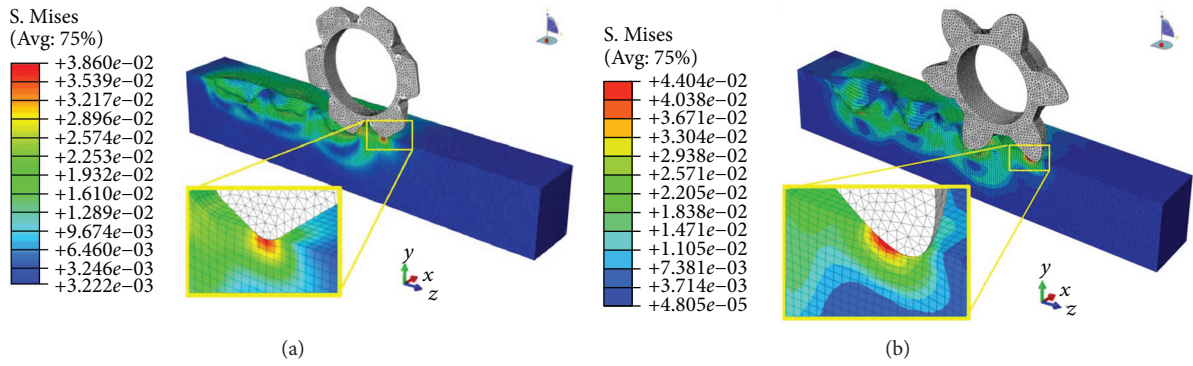


FIGURE 14: Impacting stage. (a) Conventional toothed wheel. (b) Bionic toothed wheel.

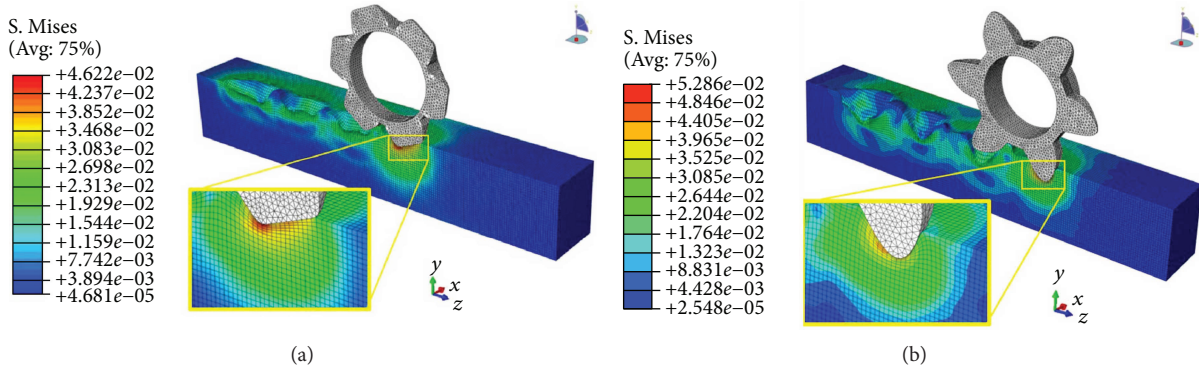


FIGURE 15: Penetrating stage. (a) Conventional toothed wheel. (b) Bionic toothed wheel.

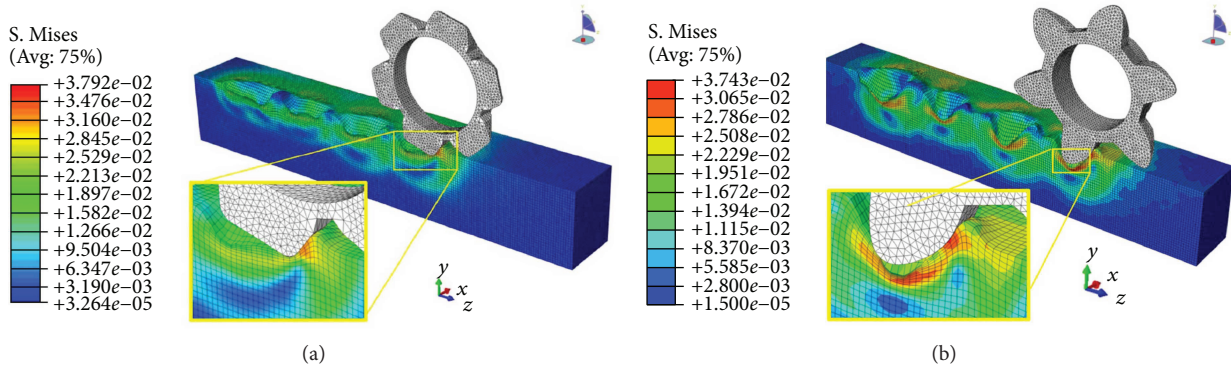


FIGURE 16: Lifting stage. (a) Conventional toothed wheel. (b) Bionic toothed wheel.

(4) Investigating mechanisms of different toothed wheel interactions' behavior with soil by finite element method, it was found that at the impacting and penetrating stages, the geometrical curvature of the outer contour curve in the bionic tooth has the ability to maximize stress concentrations in soil; the stress concentration increased by 14.1% and 14.4%, respectively. The sharp corners at the tip of the bionic tooth induced sudden increases in the stress at points near the stress raisers, which has resulted in a localized increase in stress; such stress concentrating within the soil increased the tendency of soil material to fail, thus "consolidating" the soil as opposed to

"compacting" the soil under load. In addition, the bionic toothed wheel has less stress concentration at the lifting stage, which was reduced by 11.8%. Thus, it can be more easily uplifted from the soil. Thus, required draft force is reduced and soil imprinting quality is enhanced.

Above all, the digging limb shape along with digging behavior is well inherited by the bionic toothed wheel, rolling over the soil surface and imprinting soil, just like a dung beetle waving its foreleg back and forth to dig the soil. The bionic toothed wheel requires less draft force for operating as compared with the conventional toothed wheel and imprinted

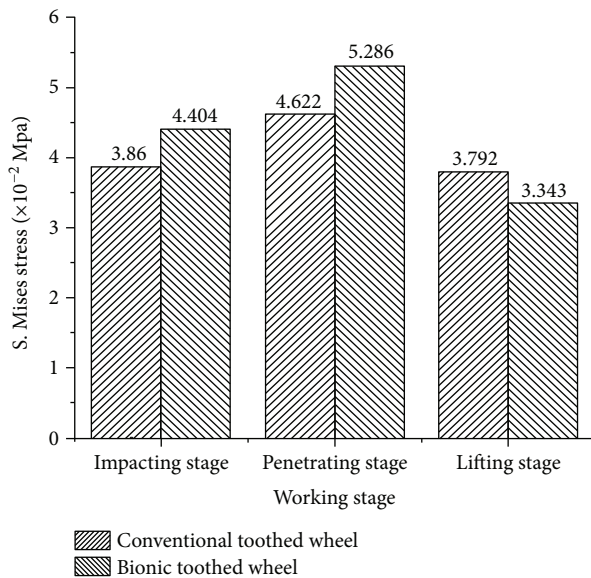


FIGURE 17: Maximum stress of conventional and bionic toothed wheel at the different working stages.

microbasin with increased water harvesting capacity. Based on its larger depression volume and less required draft force, the bionic toothed wheel would be the preferred option when undertaking a soil imprinting operation. In addition to the above considerations, the bionic toothed wheel would be convenient to manufacture locally by the widely used manufacturing technology, thus potentially increasing its availability and popularizing prospect. In addition, the special outer contour curve is useful for the design of new soil-engaging implements adapted to each type of soil for working quality enhancement and forward resistance reduction.

Conflicts of Interest

The authors declare that they have no conflicts of interest.

Acknowledgments

The financial supports for this research project are given by the National Natural Science Foundation of China for Young Scholars (Grant no. 51605210), by Yunnan Applied Basic Research Youth Project (Grant no. 2015FD011), by Introduced Talents Scientific Research Starting Foundation of Kunming University of Science and Technology (Grant no. 14118940), by the Scientific Research Fund Project of Yunnan Provincial Department of Education (Grant no. 2015Y079), and by the Opening Project of the Key Laboratory of Bionic Engineering (Ministry of Education) (K201621), Jilin University. The authors' grateful thanks are due to Professor Donghui Chen from Jilin University, for his helpful guidance, encouragement, and support in experiments.

References

[1] J. Barron and G. Okwach, "Run-off water harvesting for dry spell mitigation in maize (*Zea mays* L.): results from on-farm

research in semi-arid Kenya," *Agricultural Water Management*, vol. 74, no. 1, pp. 1–21, 2005.

- [2] L. Fleskens, L. Stroosnijder, M. Ouessar, and J. De Graaff, "Evaluation of the on-site impact of water harvesting in southern Tunisia," *Journal of Arid Environments*, vol. 62, no. 4, pp. 613–630, 2005.
- [3] T. Oweis and A. Hachum, "Water harvesting and supplemental irrigation for improved water productivity of dry farming systems in West Asia and North Africa," *Agricultural Water Management*, vol. 80, no. 1–3, pp. 57–73, 2006.
- [4] X. Wang, H. Wu, K. Dai et al., "Tillage and crop residue effects on rainfed wheat and maize production in northern China," *Field Crops Research*, vol. 132, pp. 106–116, 2012.
- [5] H. M. Salem, C. Valero, M. Á. Muñoz, M. Gil-Rodríguez, and P. Barreiro, "Effect of reservoir tillage on rainwater harvesting and soil erosion control under a developed rainfall simulator," *Catena*, vol. 113, pp. 353–362, 2014.
- [6] G. Brhane, C. S. Wortmann, M. Mamo, H. Gebrekidan, and A. Belay, "Micro-basin tillage for grain sorghum production in semiarid areas of Northern Ethiopia," *Agronomy Journal*, vol. 98, no. 1, pp. 124–128, 2006.
- [7] T. M. Boers and J. Ben-Asher, "A review of rainwater harvesting," *Agricultural Water Management*, vol. 5, no. 2, pp. 145–158, 1982.
- [8] Z. Zhang, X. Wang, J. Tong et al., "Quantification of micro-topographical preparation on soil erosion control in red soil slope surfaces," *Journal of Drainage and Irrigation Machinery Engineering*, vol. 35, no. 8, pp. 700–708, 2017.
- [9] P. Fox and J. Rockström, "Water-harvesting for supplementary irrigation of cereal crops to overcome intra-seasonal dry-spells in the Sahel," *Physics and Chemistry of the Earth, Part B: Hydrology, Oceans and Atmosphere*, vol. 25, no. 3, pp. 289–296, 2000.
- [10] P. R. Ojasvi, R. K. Goyal, and J. P. Gupta, "The micro-catchment water harvesting technique for the plantation of jujube (*Zizyphus mauritiana*) in an agroforestry system under arid conditions," *Agricultural Water Management*, vol. 41, no. 3, pp. 139–147, 1999.
- [11] K. WARD and C. CARR, *Soil Conditioning Device*, U.S. Patent and Trademark Office, US, 2010.
- [12] C. Patrick, C. Kechavarzi, I. T. James, M. O'Dogherty, and R. J. Godwin, "Developing reservoir tillage technology for semi-arid environments," *Soil Use and Management*, vol. 23, no. 2, pp. 185–191, 2007.
- [13] M. Abo-Elnor, R. Hamilton, and J. T. Boyle, "Simulation of soil-blade interaction for sandy soil using advanced 3D finite element analysis," *Soil and Tillage Research*, vol. 75, no. 1, pp. 61–73, 2004.
- [14] J. Li, Y. Yan, B. Chirende, X. Wu, Z. Wang, and M. Zou, "Bionic design for reducing adhesive resistance of the ridger inspired by a boar's head," *Applied Bionics and Biomechanics*, vol. 2017, Article ID 8315972, 10 pages, 2017.
- [15] M. Li, Y. Yang, L. Guo, D. Chen, H. Sun, and J. Tong, "Design and analysis of bionic cutting blades using finite element method," *Applied Bionics and Biomechanics*, vol. 2015, Article ID 471347, 7 pages, 2015.
- [16] Z. Zhang, J. Tong, D. Chen et al., "Bionically inspired serrated structure for improving efficiency of micro-topography preparation," *International Agricultural Engineering Journal*, vol. 24, no. 4, pp. 11–23, 2015.

- [17] M. H. Dickinson, "Bionics: biological insight into mechanical design," *Proceedings of the National Academy of Sciences of the United States of America*, vol. 96, no. 25, pp. 14208–14209, 1999.
- [18] Y. Y. Lu, "Significance and progress of bionics," *Journal of Bionics Engineering*, vol. 1, no. 1, pp. 1–3, 2004.
- [19] W. Ji, D. Chen, H. Jia, and J. Tong, "Experimental investigation into soil-cutting performance of the claws of mole rat (*Scaptochirus moschatus*)," *Journal of Bionic Engineering*, vol. 7, pp. S166–S171, 2010.
- [20] K. Tian, X. Li, B. Zhang, Q. Chen, C. Shen, and J. Huang, "Design and test research on cutting blade of corn harvester based on bionic principle," *Applied Bionics and Biomechanics*, vol. 2017, Article ID 6953786, 8 pages, 2017.
- [21] M. Li, D. H. Chen, S. J. Zhang, and J. Tong, "Biomimetic design of a stubble-cutting disc using finite element analysis," *Journal of Bionic Engineering*, vol. 10, no. 1, pp. 118–127, 2013.
- [22] L. Xu, M. X. Lin, J. Q. Li, Z. L. Wang, and B. Chirende, "Three-dimensional geometrical modelling of wild boar head by reverse engineering technology," *Journal of Bionic Engineering*, vol. 5, no. 1, pp. 85–90, 2008.
- [23] T. F. Shao, L. B. Zhang, M. Y. Du, G. J. Bao, and Q. H. Yang, "Fruit harvesting continuum manipulator inspired by elephant trunk," *International Journal of Agricultural and Biological Engineering*, vol. 8, no. 1, pp. 57–63, 2015.
- [24] X. R. Zhang, C. Wang, Z. S. Chen, and Z. W. Zeng, "Design and experiment of a bionic vibratory subsoiler for banana fields in southern China," *International Journal of Agricultural and Biological Engineering*, vol. 9, no. 6, pp. 75–83, 2016.
- [25] S. Liu, S. Weng, Y. Liao, and D. Zhu, "Structural bionic design for digging shovel of cassava harvester considering soil mechanics," *Applied Bionics and Biomechanics*, vol. 11, no. 1–2, pp. 1–11, 2014.
- [26] Z. Y. Chang, W. Liu, J. Tong et al., "Design and experiments of biomimetic stubble cutter," *Journal of Bionic Engineering*, vol. 13, no. 2, pp. 335–343, 2016.
- [27] L. Xue, R. R. Zhang, W. Zong, J. F. Song, and M. Zou, "Bionic design for Mars sampling scoop inspired by Himalayan Marmot Claw," *Applied Bionics and Biomechanics*, vol. 2016, Article ID 5713683, 9 pages, 2016.
- [28] S. Li, J. Tong, S. Zhang, and B. Chen, "Reverse engineering and engineering bionics," *Transactions of the Chinese Society for Agricultural Machinery*, vol. 35, no. 2, pp. 109–112, 2004.
- [29] R. C. Gonzalez and R. E. Woods, *Digital Image Processing*, Prentice Hall, New Jersey, 3rd edition, 2008.
- [30] M. A. El-Sayed and A. New Algorithm, "Based entropic threshold for edge detection in images," *International Journal of Computer Science Issues*, vol. 8, no. 5, 2011.
- [31] A. El-Zaart and A. Novel Method, "For edge detection using 2 dimensional gamma distribution," *Journal of Computer Science*, vol. 6, no. 2, pp. 199–204, 2010.
- [32] H. Jia, C. Li, Z. Zhang, and G. Wang, "Design of bionic saw blade for corn stalk cutting," *Journal of Bionic Engineering*, vol. 10, no. 4, pp. 497–505, 2013.
- [33] H. Bentaher, A. Ibrahmi, E. Hamza et al., "Finite element simulation of moldboard–soil interaction," *Soil and Tillage Research*, vol. 134, no. 0, pp. 11–16, 2013.
- [34] M. Abo-Elnor, R. Hamilton, and J. T. Boyle, "3D dynamic analysis of soil–tool interaction using the finite element method," *Journal of Terramechanics*, vol. 40, no. 1, pp. 51–62, 2003.
- [35] J. Tong, Z. Zhang, D. Chen, Q. Zhang, and Y. Ma, "Three-dimensional dynamic finite element analysis of interaction between toothed wheel and soil," *Transactions of the Chinese Society of Agricultural Engineering*, vol. 30, no. 10, pp. 48–58, 2014.
- [36] T. Keller, M. Berli, S. Ruiz et al., "Transmission of vertical soil stress under agricultural tyres: comparing measurements with simulations," *Soil and Tillage Research*, vol. 140, pp. 106–117, 2014.
- [37] T. Keller and J. Arvidsson, "A model for prediction of vertical stress distribution near the soil surface below rubber-tracked undercarriage systems fitted on agricultural vehicles," *Soil and Tillage Research*, vol. 155, pp. 116–123, 2016.

Research Article

Crashworthiness Design for Bionic Bumper Structures Inspired by Cattail and Bamboo

Tao Xu,¹ Nian Liu,¹ Zhenglei Yu,² Tianshuang Xu,¹ and Meng Zou²

¹School of Mechanical Science and Engineering, Jilin University, Changchun, China

²Key Lab of Bionic Engineering, Ministry of Education, Jilin University, Changchun, China

Correspondence should be addressed to Zhenglei Yu; yuzhenglei@hotmail.com

Received 28 April 2017; Revised 17 August 2017; Accepted 19 September 2017; Published 8 October 2017

Academic Editor: Saurabh Das

Copyright © 2017 Tao Xu et al. This is an open access article distributed under the Creative Commons Attribution License, which permits unrestricted use, distribution, and reproduction in any medium, provided the original work is properly cited.

Many materials in nature exhibit excellent mechanical properties. In this study, we evaluated the bionic bumper structure models by using nonlinear finite element (FE) simulations for their crashworthiness under full-size impact loading. The structure contained the structural characteristics of cattail and bamboo. The results indicated that the bionic design enhances the specific energy absorption (SEA) of the bumper. The numerical results showed that the bionic cross-beam and bionic box of the bionic bumper have a significant effect on the crashworthiness of the structure. The crush deformation of bionic cross-beam and box bumper model was reduced by 33.33%, and the total weight was reduced by 44.44%. As the energy absorption capacity under lateral impact, the bionic design can be used in the future bumper body.

1. Introduction

In traffic accidents, the bumper, side-door beam, and B-pillar of a car can absorb the impact of energy to ensure the safety of drivers and passengers. The bumper suffers from a lateral impact loading during the impact process. The primary function of a bumper is to attenuate the effects of a collision in direct contact [1]. Typically, the bumper of a car consists of four different parts: the fascia, the cross-beam, the crash box, and the crushable column [2]. The cross-beam under the bumper is usually loaded as a thin-walled section of the lateral compression (Figure 1). A lot of research has been carried out on the thin-walled structure in the process of straightening the horizontal compression [3]. The thin-walled structures are used as a good energy absorber in experimental investigation, analysis, and numerical methods.

Liu [4] had investigated numerically the conventional polygonal thin-walled columns with rectangular, octagonal, and curved hexagonal columns, in both quasi-static axial and lateral load conditions. Ahmad and Thambiratnam [5] had found that the conical tube filled with foam had better

energy absorption performance than the empty conical tube. Under the axis compression conditions, Fan et al. [6] studied the hexagonal, octagonal, 12-sided, and 16-sided tubes experimentally and numerically. The results pointed out that the number of corners were directly related to energy absorption. Within a certain range, an increase in number of corners of the thin-walled column could help to improve energy absorption. Shen et al. [7] had studied the lateral crushing behavior of two concentric aluminum tubes of different diameters which were filled with aluminum foam. Fang et al. [8] had investigated the energy absorption characteristics of the functionally graded foam-filler into rectangular columns in transverse impact loading.

Some researcher had introduced the special cross sections of thin-walled structures as energy absorbers under various load conditions [9–11]. Loughlan et al. [12] had determined the coupled local distortions of thin-walled channel segments using finite element model. Alavi Nia and Parsapour [13] had investigated the mechanical behavior of the triangular, square, hexagonal, and octagonal sections of the thin-walled tubes under the quasi-static axial loading. Under quasi-static lateral loading, Baroutaji et al. [14] used the response surface

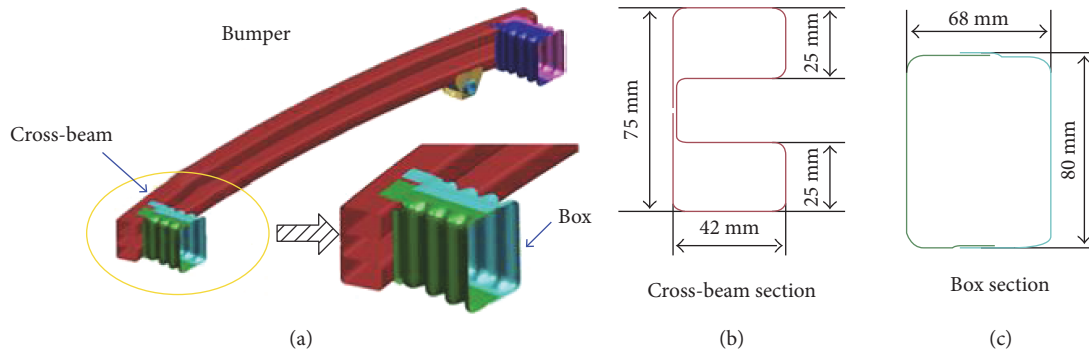


FIGURE 1: The FE model of bumper: (a) detail with enlarged scale, (b) the section of cross-beam, and (c) the section of crash box.

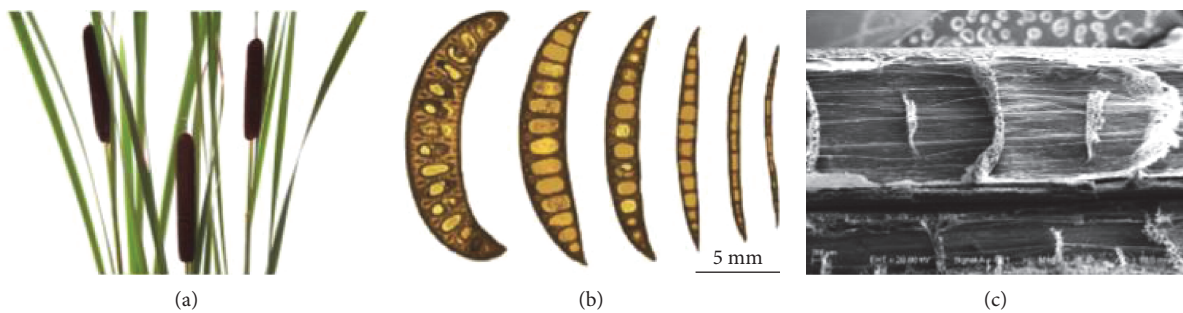


FIGURE 2: Cattail plants: (a) plants in the wild, (b) cross sections of an emergent leaf from the base to the apex, and (c) microstructures of an emergent leaf observed using SEM [19].

and optimization methods to solve thin-walled rectangular tube energy absorption problem.

The thin wall structure studies in the abovementioned literature has a simple cross section. The complex cross sections of the thin-walled structures may have better crashworthiness than existing ones, but it remains an open challenge for researchers how to design a thin-walled structure with better crash performance and ease of production. After billions of years of evolution, some biological structures already have excellent properties and ingenious frameworks, which can provide inspiration to thin-walled structure designers.

Nowadays, bionic structures have gained the attention of researchers due to their excellent crash performance and very light weight. Bamboo [15, 16], horsetails [17, 18], and cattail [19] are kinds of gradient composite material with good mechanical properties in the natural environment. Due to bamboo's low density, it has a higher stiffness-mass ratio than some metallic materials such as steel and aluminum. The structural characteristics of horsetails lie in the cylindrical multi-cell structure which has good bending resistance. The emergent leaves exhibited a high slenderness ratio and a distinct twisting chiral morphology. It was found that the leaves have evolved multiscale structures and superior mechanical properties, both of which feature functionally gradient variations, to improve their resistance to failure. Various studies related to macrostructures and microstructures had shown that the gradient distribution of the plant has excellent mechanical properties [20–23].

Bionic structure could have better crashworthiness than traditional thin-walled structure when it is under the lateral dynamic loading. However, to the best of our knowledge, there are few studies on the crashworthiness of bionic structure under the condition of lateral dynamic loading [24–26].

In this work, two kinds of bionic structures was imitated: the structural characteristics of bamboo and cattail. We created a finite element (FE) model for the impact and validated our results with experiments. We simulated the process of energy absorption under axial/lateral loading and drop impact by using nonlinear finite element code LS-DYNA. The results showed that the design of bionic structure could be further improved for better crashworthiness and structural behaviors.

2. Bionic Design

In the nature, the biological structure need to adapt the surrounding environment. Many structures are lightweight along with good mechanical properties which can transport water and nutrients from root to leaf [27].

2.1. Cattail and Bamboo Plant. Cattail is also called Typha, which is an herbaceous perennial emergent aquatic macrophyte (Figure 2). They mainly inhabit streams, lakes, marshes, rivers, reservoirs, ditches, freshwater ponds, canals, and other shallow water areas [28, 29]. Due to its wide distribution and properties, the stems and leaves can

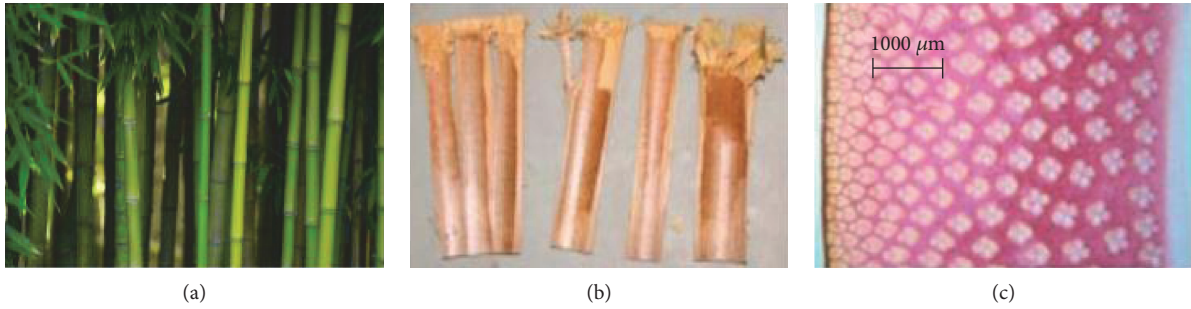


FIGURE 3: Bamboo: (a) collection site of bamboo, (b) internode samples, and (c) cross section [15, 16].

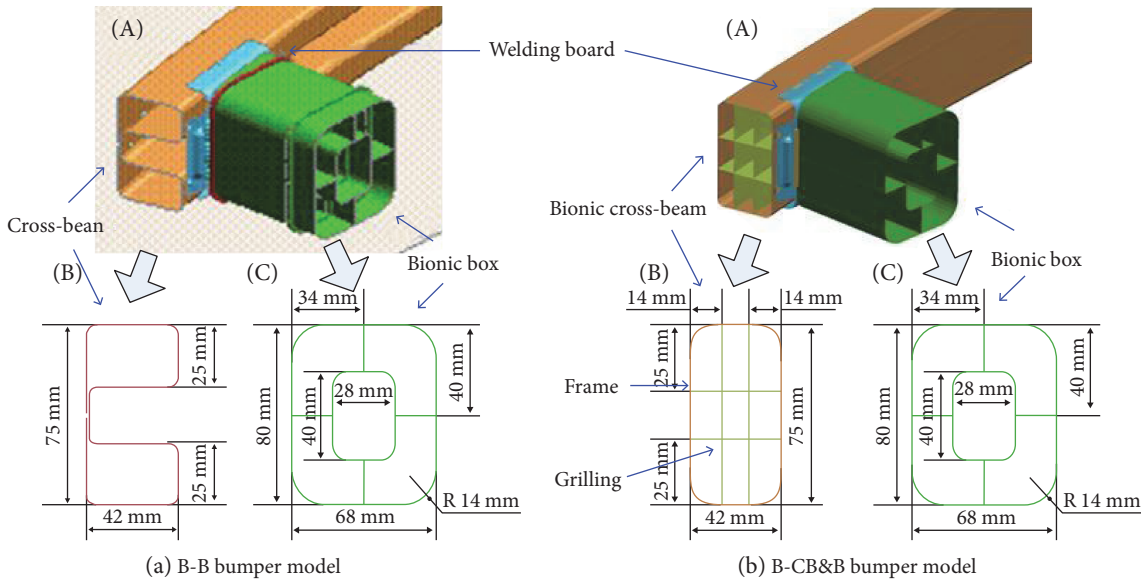


FIGURE 4: The bionic bumper models: (a) B-B bumper model and (b) B-CB&B bumper model.

be used as raw materials for candle cores, paper, ropes, and woven fabrics.

In order to understand the influence of chirality on cattail’s mechanical behavior, the researchers investigated the twisted chiral morphology and the wind adaptation of banana leaves by experiment. From Figure 2(c), their multiscale structures had been observed using optical microscope, which have superior mechanical properties. It was found that the leaves have evolved multiscale structures and superior mechanical properties, both of which feature functionally gradient variations, to improve their ability of lodging resistance. The synergistic effect of chiral morphology and reconfiguration could greatly improve the survivability of cattail plants in the wind [19].

Bamboo is a typical tubular structure with good mechanical properties in the natural environment. They have a multilayered composite structure from the cellular level to the tissue level [30] (Figure 3). The excellent mechanical properties of bamboo depends on the hollowness, tubular shape, discrete distribution of the nodes, gradient distribution of the vascular bundles, and multilayer structure of the chondrocytes [20]. A large number of voids between the organizations make bamboo prone to splitting during axial

loading which results in a reduction in the energy absorption of bamboo.

In this work, the cattail was used to design the bionic cross-beam structure and bamboo was the prototype of the bionic energy box.

2.2. Bionic Cross-Beam and Bionic Energy Box Design. In Figure 2(b), the internal rib structure of cattail can be a very good resistance to external pressure. According to its structural and functional characteristics, a bionic cross-beam with the structure of the cappuccino was designed (Figure 4(b), (B)).

In Figure 3(c), we showed the macroscopic structures of bamboo. The load was delivered by vascular bundles in the bamboo, which were connected with ground tissue (serving as a matrix). Therefore, the structure and function of these matrices were applied to the bionic structure to improve the load transfer and energy absorption efficiency. A bionic matrix designed to connect bionic cross-beam and transport loads is called a bionic box (Figure 4(a), (C)).

Bamboo has excellent bending and compressive properties, preventing the cracking phenomenon during the vertical and horizontal compression loading [25]. Hence, a welding

TABLE 1: The parameters of models.

Model	Component	Part	Material	Thickness (mm)
Initial bumper	Cross-beam		High-strength steel (trip800)	1.8
	Box		High-strength steel (st280)	1.8
	Cross-beam		High-strength steel (trip800)	1.8
B-B bumper	Box		Extrusion aluminum (6062T6)	1.5
	Welding plate		High-strength steel (st280)	1.4
	Cross-beam	Frame	Extrusion aluminum (6062T6)	2.0
B-B&CB bumper		Grilling	Extrusion aluminum (6062T6)	1.7
	Box		Extrusion aluminum (6062T6)	1.5
	Welding plate		High-strength steel (st280)	1.4

plate was designed as a bionic node reinforcement rib for a bionic bumper structure.

Based on the relationship between the structure and the dynamic mechanical properties of cattail and bamboo, three components of bionic structures (i.e., bionic cross-beam, bionic box, and welding board) were designed. Two bionic bumper models, namely, bio-box bumper (B-B bumper) and bio-cross-beam and bio-box bumper (B-CB&B bumper) were developed by combining the different bionic components (Figure 4). The parameters of the bionic cross-beam, bionic box, and welding board are shown in Figure 4, and the structural parameters of the bionic structure are listed in Table 1. Bionic cross-beam and bionic box adopted the extrusion aluminum instead of high-strength steel to reduce the total weight. The materials were all the standard types which can be purchased from the suppliers.

3. Numerical Model

3.1. Structural Crashworthiness Criteria. Properly defined crash performance standards are critical to the evaluation of the crash bionic bumper. The widely use concept in collision standards are energy absorption (EA, kJ), mean crushing force (MCF, N), and specific energy absorption (SEA, kJ/N). SEA denotes the energy absorbed per unit mass of the absorber, which is often used to estimate the energy absorption capabilities of the structures.

$$SAE = \frac{EA}{M}, \quad (1)$$

where M represents the total mass of the structure. EA represents the energy absorption in crash, which can be formulated as

$$EA = \int_0^s F(x)dx, \quad (2)$$

where s represents the crash displacement and F denotes the impact force. From (2), it can be seen that the SEA value is higher for the design of the energy absorption structure that has better energy absorption capability in the collision process.

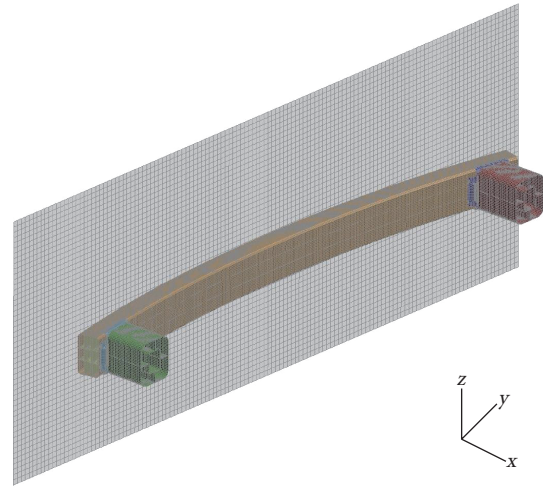


FIGURE 5: The meshing of the B-B bumper FE model.

3.2. FE Modeling Method. The finite element models were developed using Hypermesh 14.0, and the collision analysis was carried out using commercial code LS-DYNA. Shell elements were used to set the wall. In this work, the material failure of aluminum alloy tube was not considered. It was not necessary that the smaller grid size would significantly improve the accuracy of the simulation results, but it could definitely increase the computation cost. Thus, before the tests, the accuracy of the mesh was investigated. We tested force versus displacement for five different mesh sizes and adopted the element size of 2.0×2.0 mm in all our simulations. The FE model of one of the B-B bumper under lateral impact was shown in Figure 5. There were several materials such as high-strength steel and extrusion aluminum that had been used as the wall in different applications.

In this work, simulation had been performed to analyze the energy absorption effect of the bionic bumpers. It was a positive impact test, in which we used a full-size rigid wall to crush the bumper model that resembles a car in a frontal collision. All three models have been impacted by a rigid wall, and the height of the rigid wall in the impact tests was converted to the real collision. By calculating kinetic energy conservation, the full-size rigid wall's weight was 9123.3 N. The initial speed of the test was 4.33 m/s. The loading of the test

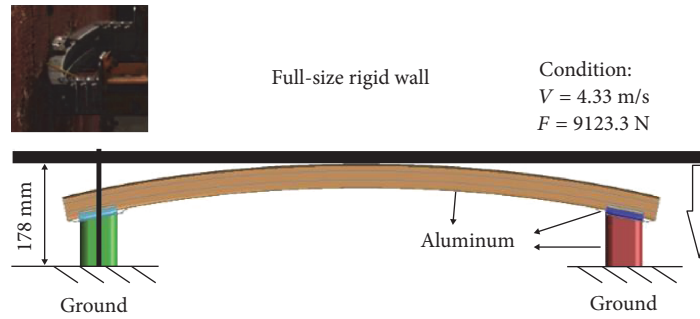


FIGURE 6: The loading condition of the full-size impact simulation.

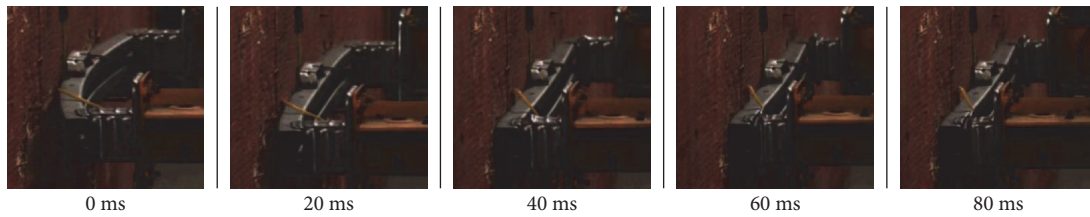


FIGURE 7: Full-size crash test of initial bumper by experiment.

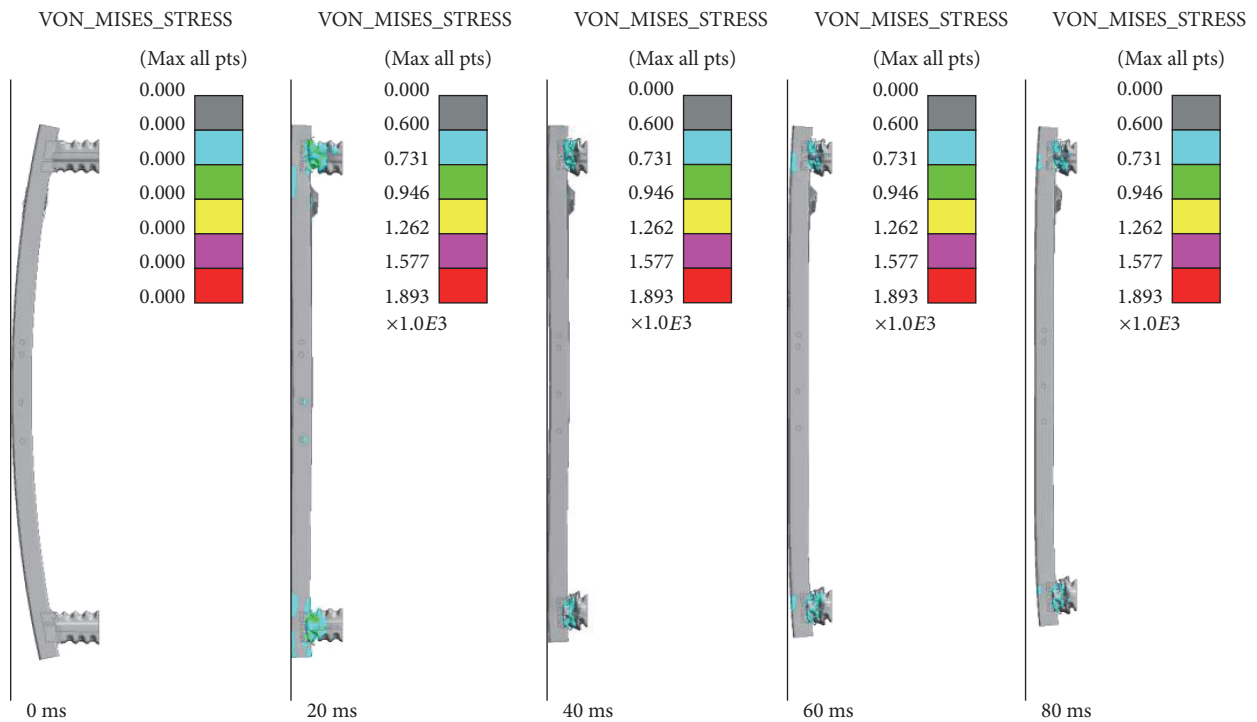


FIGURE 8: Full-size crash test of initial bumper by simulation.

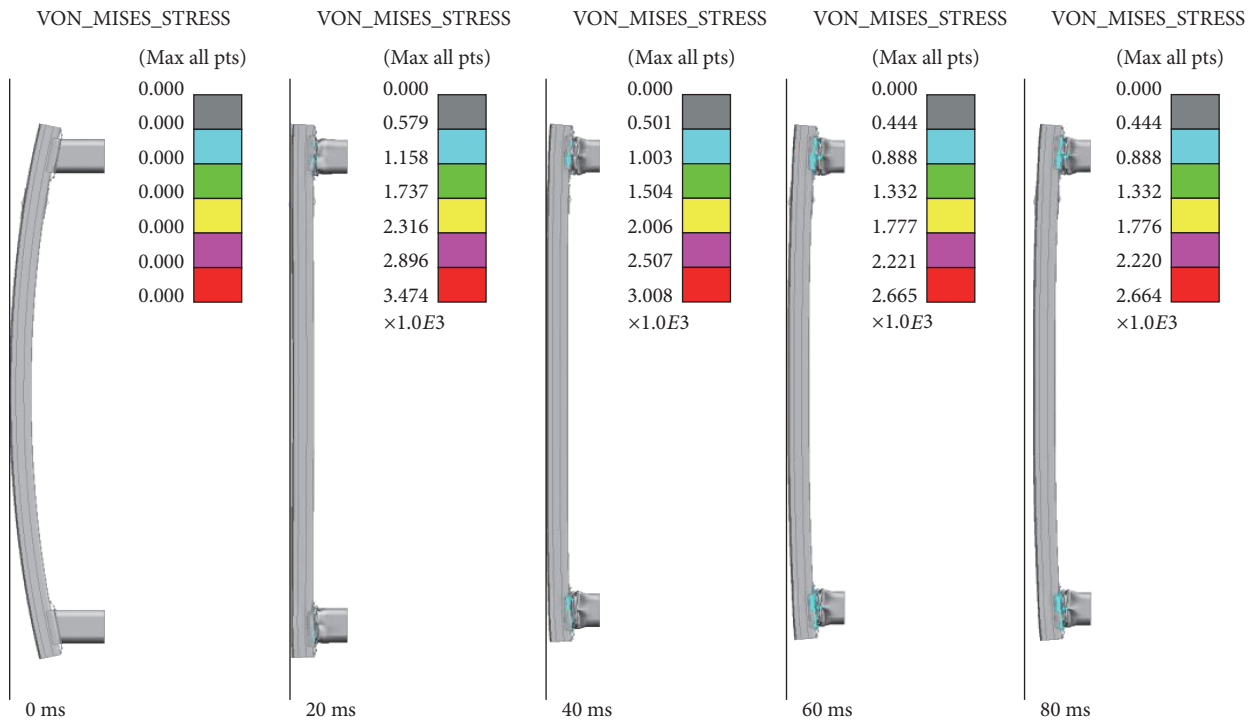
had been shown in Figure 6, and the material of components were listed in Table 1.

4. Numerical Simulation and Analysis

4.1. Validation of the FE Model. Frontal crash test was one of the main tests to verify the passive safety performance of

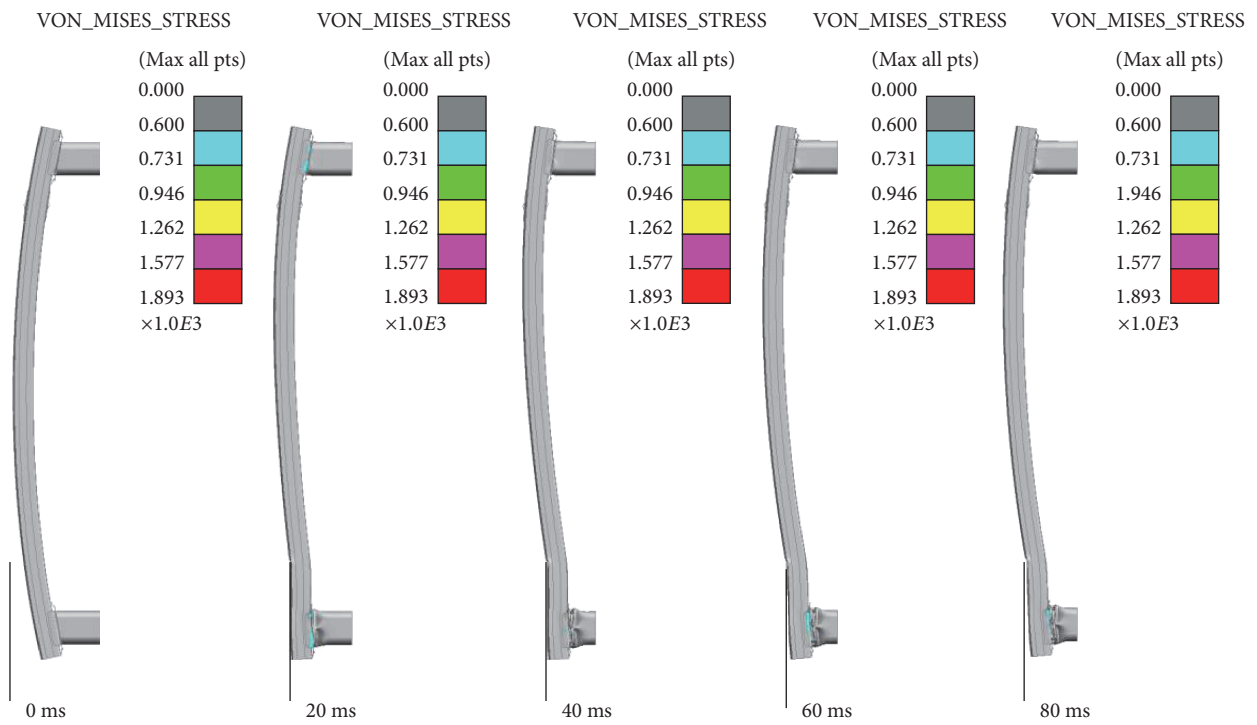
vehicles [31]. The bumper of a car was tested under the condition of a frontal crash. In this experiment, the initial bumper impacted onto the rigid wall at 4.4 m/s. To validate the FE models, the bumper model with the same geometry, shape, and loading condition as the experiment was developed and simulated. Thus, the experimental results validated the finite element model in this study.

B-B bumper model



(a)

B-CB and B bumper model



(b)

FIGURE 9: Full-size crash test of two bionic bumper models by simulation: (a) the result of B-B bumper model and (b) the result of B-CB&B bumper model.

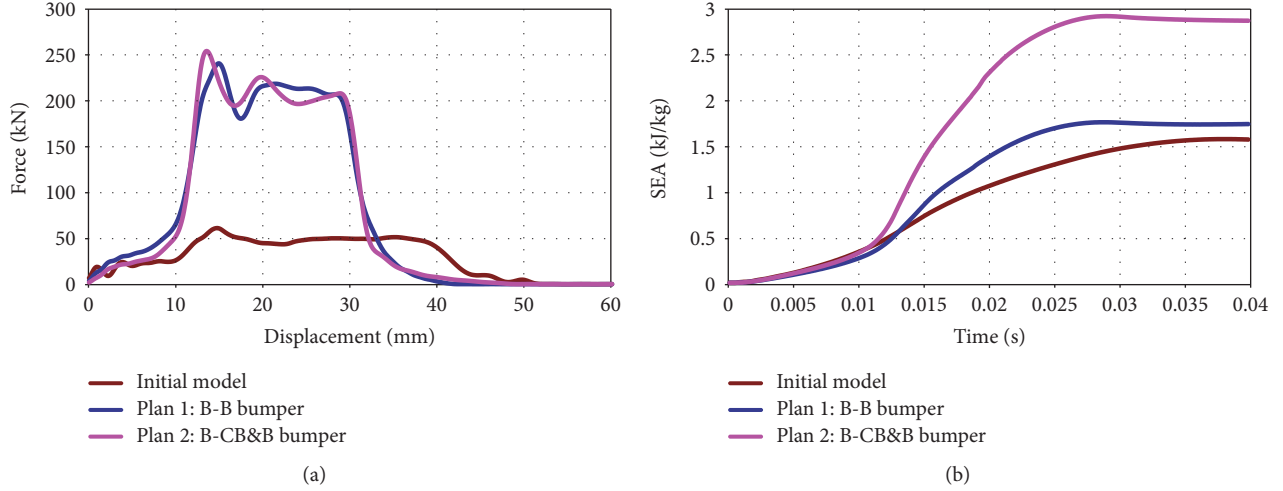


FIGURE 10: Crashworthiness characteristics associated with full-size crash to the bumper models: (a) lead-displacement curve and (b) SEA-time curve.

In Figure 7, we showed the distortion of bumper during the collision process, which was shot by high-speed camera. From 0 to 40 ms, cross-beam absorbed impact energy and produced large plastic deformation. From 40 to 60 ms, the collision energy was transmitted to the box which produced plastic deformation. After 60 ms, the structure was destroyed by the impact which could not absorb any impact energy. Figure 8 displayed the FE model's comparison of crash behavior by simulation. From Figures 7 and 8, it could be seen that the simulation results were in close agreement with experimental results. Therefore, FE simulations could be used reliably to study the behavior of the bionic bumpers.

4.2. Full-Size Crash Simulation. In materials science and engineering, the von Mises stress is a scalar value of stress which can be computed from the Cauchy stress tensor [32]. It is used to predict yielding of materials under complex loading. In this case, the crushing and deformation process of the two bionic bumper structures were shown in Figure 9. From the figure, it could be seen that the absorption box had contact with the cross-beam and thus had higher Mises stress and therefore folded progressively in 20 ms. Compared with the initial bumper model, the distribution of Mises stress in two kinds of bionic structure bumper models was smaller and the crushing phenomenon had happened after 40 ms. In the B-CB&B bumper model, the bionic cross-beam also had the distribution of Mises stress, which showed that the bionic cross-beam had played the role in energy absorption. The folding patterns of the bionic cross-beam and box had played an important role in the full-size crash simulation of the new bionic bumper structure. According to the structures and mechanical behavior of the three models, the bionic cross-beam and bionic box were the main components to effectively improve the stability of the models on defending the failure of loads.

Figure 10 showed the load-displacement and SEA-time curves, respectively, for the three types of bumper models under full-size crush loading. The curve of the initial bumper

TABLE 2: Results.

Model	Energy absorption (kJ/N)	Deformation (mm)	Total weight (N)
Initial bumper	1.550	39	52.974
B-B bumper	1.785	25	49.05
B-CB&B bumper	2.837	26	29.43

was lower than that of the bionic bumper structures. The peak of the B-CB&B's curve was higher than the peak of the B-B bumper model. The results of energy absorption, deformation, and total weight were shown in Table 2. Compared with the initial bumper model, the energy absorption of B-B bumper model and B-CB&B bumper model was increased by 15.16% and 83.03%, respectively. And the crush deformation was reduced by 35.90% and 33.33%. The mechanical properties and deformation behavior of the samples indicate that the internal core structure had a great influence on the mechanical properties of the models. The separation of the cross wall with a lightweight core increased the moment of inertia of sandwich structures that could make the structure to resist the bending and buckling loads. The energy absorption of the two bionic bumper models was higher than the initial bumper model, and the deformation of the two bionic models was much smaller than the initial one [15, 16]. Comparing the two bionic bumper models, it could be seen that the B-CB&B model with multimaterial had the best energy absorption characteristics with the least weight. Inspired by the gradient distribution of cattail and bamboo, bionic cross-beam structure had compression performance and bionic energy box had bending characteristics. These results showed that the bionic structure can effectively improve the impact resistance of bumper structure.

5. Conclusion

In this study, we had investigated two bionic bumper models under full-size crash and size impact loading, with both bumpers imitating the structural characteristics of cattail and bamboo. Three FE models had been investigated on crash-worthiness using nonlinear finite element code LS-DYNA. According to the numerical results, the bionic bumper models had remarkably effected their crashworthiness. The main points concluded from this work are as follows.

- (1) Inspired by the gradient distribution of cattail and bamboo, two bionic bumper structure models had been designed, which were composed of a bionic cross-beam, a bionic box, and a welding board. The bionic cross-beam served the same function as that of the inner structure of the cattail, the bionic box acted as the matrices and vascular bundles of bamboo, and the welding board resembled the bamboo's joint.
- (2) The results showed that the bionic bumper models had better energy absorption characteristics than the initial model. The BCB&B bumper had the best energy absorption characteristics. Meanwhile, the crush deformation was reduced by 33.33% and the total weight was reduced by 44.44% for the bionic bumper model.
- (3) The numerical results showed that the bionic bumper structure exhibited potential advantage of energy-absorbing capabilities under conditions of full-size impact. However, the bionic structure needs further studies to explore the complex structure of cattail and bamboo. The bionic structure can be used as an energy absorber in vehicle bodies and other engineering applications.

Conflicts of Interest

The authors declare no conflicts of interest.

Acknowledgments

The authors would like to acknowledge the National Natural Science Funds for Distinguished Young Scholars (Grant no. 51505181), the China Postdoctoral Science Foundation funded project (no. 2016M590256), and the Technology Development of Jilin Province (no. 20150520106JH).

References

- [1] M. El-Sadig and H. El Kadi, "Crushing behavior of laterally compressed composite elliptical tubes: experiments and predictions using artificial neural networks," *Composite Structures*, vol. 83, pp. 399–412, 2008.
- [2] M. M. Davoodi, S. M. Sapuan, and R. Yunus, "Conceptual design of a polymer composite automotive bumper energy absorber," *Materials & Design*, vol. 29, pp. 1447–1452, 2008.
- [3] A. Niknejad and P. H. Orojloo, "A novel nested system of tubes with special cross-section as the energy absorber," *Thin-Walled Structures*, vol. 100, pp. 113–123, 2016.
- [4] Y. Liu, "Crashworthiness design of multi-corner thin-walled columns," *Thin-Walled Structures*, vol. 46, no. 12, pp. 1329–1337, 2008.
- [5] Z. Ahmad and D. P. Thambiratnam, "Crushing response of foam-filled conical tubes under quasi-static axial loading," *Materials & Design*, vol. 30, no. 7, pp. 2393–2403, 2009.
- [6] Z. Fan, G. Lu, and K. Liu, "Quasi-static axial compression of thin-walled tubes with different cross-sectional shapes," *Engineering Structures*, vol. 55, pp. 80–89, 2013.
- [7] J. Shen, G. Lu, D. Ruan, and C. C. Seah, "Lateral plastic collapse of sandwich tubes with metal foam core," *International Journal of Mechanical Sciences*, vol. 91, pp. 99–109, 2015.
- [8] J. Fang, Y. Gao, G. Sun, Y. Zhang, and Q. Li, "Parametric analysis and multi objective optimization for functionally graded foam-filled thin-wall tube under lateral impact," *Computational Materials Science*, vol. 90, pp. 265–275, 2014.
- [9] M. Seitzberger, F. G. Rammerstorfer, R. Gradinger, H. P. Degischer, M. Blaimschein, and C. Walch, "Experimental studies on the quasi-static axial crushing of steel columns filled with aluminium foam," *International Journal of Solids and Structures*, vol. 37, no. 30, pp. 4125–4147, 2000.
- [10] W. G. Chen, "Experimental and numerical study on bending collapse of aluminum foam-filled hat profiles," *International Journal of Solids and Structures*, vol. 38, no. 44–45, pp. 7919–7944, 2011.
- [11] Z. H. Zhang, S. T. Liu, and Z. L. Tang, "Design optimization of cross-sectional configuration of rib-reinforced thin-walled beam," *Thin-Walled Structures*, vol. 47, pp. 868–878, 2009.
- [12] J. Loughlan, N. Yidris, and K. Jones, "The failure of thin-walled lipped channel compression members due to coupled local-distortional interactions and material yielding," *Thin-Walled Structures*, vol. 61, pp. 14–21, 2012.
- [13] A. Alavi Nia and M. Parsapour, "Comparative analysis of energy absorption capacity of simple and multi-cell thin-walled tubes with triangular, square, hexagonal and octagonal sections," *Thin-Walled Structures*, vol. 74, pp. 155–165, 2014.
- [14] A. Baroutaji, E. Morris, and A. G. Olabi, "Quasi-static response and multi-objective crashworthiness optimization of oblong tube under lateral loading," *Thin-Walled Structures*, vol. 82, pp. 262–277, 2014.
- [15] M. Zou, S. C. Xu, C. G. Wei, H. X. Wang, and Z. Z. Liu, "A bionic method for the crashworthiness design of thin-walled structures inspired by bamboo," *Thin-Walled Structures*, vol. 101, pp. 222–230, 2016.
- [16] M. Zou, C. G. Wei, J. Q. Li, S. C. Xu, and X. Zhang, "The energy absorption of bamboo under dynamic axial loading," *Thin-Walled Structures*, vol. 95, pp. 255–261, 2015.
- [17] L. B. Duan, G. Y. Sun, J. J. Cui, T. Chen, A. G. Cheng, and G. Y. Li, "Crashworthiness design of vehicle structure with tailor rolled blank," *Structural and Multidisciplinary Optimization*, vol. 53, pp. 321–338, 2016.
- [18] F. X. Xu, G. Y. Sun, G. Y. Li, and Q. Li, "Crashworthiness design of multi-component tailor-welded blank (TWB) structures," *Structural and Multidisciplinary Optimization*, vol. 48, pp. 653–667, 2013.
- [19] Z. L. Zhao, W. X. Huang, B. W. Li et al., "Synergistic effects of chiral morphology and reconfiguration in cattail leaves," *Journal of Bionic Engineering*, vol. 12, pp. 634–642, 2015.

- [20] U. G. Wegst, "Bending efficiency through property gradients in bamboo, palm, and wood-based composites," *Journal of the Mechanical Behavior of Biomedical Materials*, vol. 4, pp. 744–755, 2011.
- [21] T. Tan, N. Rahbar, S. M. Allameh et al., "Mechanical properties of functionally graded hierarchical bamboo structures," *Acta Biomaterialia*, vol. 7, pp. 3796–3803, 2011.
- [22] A. K. Ray, S. Mondal, S. K. Das, and P. Ramachandrarao, "Bamboo—a functionally graded composite correlation between microstructure and mechanical strength," *Journal of Materials Science*, vol. 40, pp. 5249–5253, 2005.
- [23] F. Wang, Z. Shao, and Y. Wu, "Mode II interlaminar fracture properties of Moso bamboo," *Composites Part B: Engineering*, vol. 44, pp. 242–247, 2013.
- [24] S. Liu, Z. Tong, Z. Tang, Y. Liu, and Z. Zhang, "Bionic design modification of non-convex multi-corner thin-walled columns for improving energy absorption through adding bulkheads," *Thin-Walled Structures*, vol. 88, pp. 70–81, 2015.
- [25] H. Jiao, Y. Zhang, and W. Chen, "The lightweight design of low RCS pylon based on structural bionics," *Journal of Bionic Engineering*, vol. 7, no. 2, pp. 182–190, 2010.
- [26] L. Zhao, J. Ma, W. Chen, and H. Guo, "Lightweight design and verification of gantry machining center crossbeam based on structural bionics," *Journal of Bionic Engineering*, vol. 8, no. 2, pp. 201–206, 2011.
- [27] M. Milwich, T. Speck, O. Speck, T. Stegmaier, and H. Planck, "Biomimetics and technical textiles: solving engineering problems with the help of nature's wisdom," *American Journal of Botany*, vol. 93, no. 10, pp. 1455–1465, 2006.
- [28] J. F. Morton, "Cattails (*Typha* spp.)—weed problem or potential crop?," *Economic Botany*, vol. 29, pp. 7–29, 1975.
- [29] J. B. Grace and J. S. Harrison, "The biology of Canadian weeds. 73. *Typha-latifolia* L., *Typha-angustifolia* L. and *Typha-xglauca* Godr," *Canadian Journal of Plant Science*, vol. 66, pp. 361–379, 1986.
- [30] H. P. S. A. Khalil, I. U. H. Bhat, M. Jawaid, A. Zaidon, D. Hermawan, and Y. S. Hadi, "Bamboo fibre reinforced biocomposites: a review," *Materials & Design*, vol. 42, pp. 353–368, 2012.
- [31] Y. Tanaka, H. Yonezawa, Y. Matsui, N. Hosokawa, and K. Mizuno, "Car-to-car side impact tests in various conditions," SAE 2010 World Congress & Exhibition, SAE Technical Paper 2010-01-1159, Detroit, MI, USA, 2010.
- [32] R. von Mises, "Mechanik der festen Körper im plastisch deformablen Zustand," *Göttingen Nachrichten Math Physica*, vol. 1, pp. 582–592, 1913.

Research Article

Study on Effects of Titanium Surface Microporous Coatings Containing Zinc on Osteoblast Adhesion and Its Antibacterial Activity

Quan-ming Zhao,¹ Guang-zhong Li,² Hao-ming Zhu,¹ and Li Cheng¹

¹Department of Orthopedic Surgery, Wuxi People's Hospital, Nanjing Medical University, Wuxi City, Jiangsu Province 214023, China

²State Key Laboratory of Porous Metal Materials, Northwest Institute for Nonferrous Metal Research, Xi'an, Shaanxi Province 710016, China

Correspondence should be addressed to Quan-ming Zhao; bsh1106@163.com

Received 15 June 2017; Accepted 22 August 2017; Published 2 October 2017

Academic Editor: Saurabh Das

Copyright © 2017 Quan-ming Zhao et al. This is an open access article distributed under the Creative Commons Attribution License, which permits unrestricted use, distribution, and reproduction in any medium, provided the original work is properly cited.

Metal surface structure/biomedical function integration is the current research focus. In previous studies, we have successfully prepared the microporous coatings containing zinc on the pure titanium surface by MAO. In the study, osteoblasts were seeded on the surface of the microporous coatings containing zinc and the adhesion of osteoblasts were evaluated, and the antibacterial activity of the microporous coatings containing zinc is observed through in vitro bacterial experiments. The result indicates that the adhesion ability of osteoblasts on the surface of microporous coatings containing zinc was very good, and the coatings could obviously inhibit the growth of *Staphylococcus aureus* and had good antibacterial activity. In conclusion, the microporous coatings containing zinc on titanium surface have good osteogenic and antibacterial properties and have good application prospect.

1. Introduction

Based on the good biocompatibility, mechanical properties, and corrosion resistance, titanium-based metal has become the first choice for the hard tissue repair and replacement, which has been widely used in clinical practice and achieved good results. But the titanium-based metal is an inert material, and its biological activity is poor after being implanted in vivo, only the mechanical combination with bone tissue can be achieved, and it is difficult to form osseointegration with the bone tissue [1]. It is also prone to result in implant-related infection after implantation [2]. In addition, the titanium-based metal will be corrosive in the body, and metal ions generated during the corrosion not only are harmful to humans but also easily lead to loosening and sinking of the implant, which not only prolongs the implant repair cycle but also affects the success rate of implantation, so it cannot fully meet the clinical needs [3]. In order to make the titanium metal to retain its excellent mechanical properties and also be equipped with good biological activity, which

can induce cell adhesion and proliferation after implantation, with good antibacterial properties, the most effective way is to perform surface modification on titanium metal [4].

Through the surface modification, preparing bioactive coatings on the surface of titanium-based metal cannot only maintain the excellent mechanical properties of titanium-based metal but also give biological activity to titanium-based metal, which is a hot spot in recent years. Microarc oxidation (MAO) is an emerging material surface modification developed in recent years. Through this technology, porous, rough ceramic film can be produced in situ of the metal surface [5]. The ceramic film increases the wear resistance, corrosion resistance, and fatigue resistance of the material, greatly improving the surface properties of the material, and because the ceramic film grows in situ of the substrate, and is closely combined with the substrate, it does not easily fall off. It is more attractive that the technology can introduce bioactive elements or antibacterial elements into the coating, greatly improving the material's biological activity, so it is widely

used in surface modification of biological materials. Zinc is an important trace element in the human body. It is involved in the structure and function of more than 300 kinds of enzymes in the body, which affects the biological behavior of cells. At the same time, zinc can activate alkaline phosphatase and promote the deposition of callus calcium salt and contribute to the formation and calcification of the bone, thereby promoting fracture healing, and more importantly, zinc has been confirmed to have a good antibacterial effect [6].

In previous studies, we have successfully prepared the microporous coatings containing zinc on the pure titanium surface by MAO. The results showed that the coating material has good surface properties, but further research on the biological behavior and antibacterial properties of the coating material is needed. Therefore, this study will investigate the adhesion of osteoblasts on the surface of microporous coatings containing zinc and the antibacterial activity of the coating material on the basis of previous studies and lay a theoretical foundation for the clinical application of the coating material.

2. Materials and Methods

2.1. Preparation of Microporous Coatings Containing Zinc on the Pure Titanium Surface. The preparation of the sample has been described in detail in the previous articles [7].

2.2. Evaluation of Adhesion and Extensibility of Osteoblasts on the Surface of Microporous Coatings Containing Zinc. The osteoblasts were inoculated into a 25 cm² cell culture flask at 2.5 × 10⁴/cm², and 5 ml of α-MEM medium was added to the culture flask. The cells were incubated in a 5% carbon dioxide incubator at 37°C. After cell growth and fusion, the passage was prepared and the old medium was discarded, and after PBS rinsing, the appropriate amount of 0.25% trypsin-0.02% EDTA was added for digestion. The passage began after the medium neutralized the trypsin.

When the third generation of osteoblasts was cultured to 80% of cell fusion, the appropriate amount of 0.25% trypsin-0.02% EDTA was added for digestion, and the trypsin was neutralized and blown into cell suspension, to prepare into a certain concentration of the cell suspension. And then the osteoblasts were cultured in a cell culture plate coated with zinc ion microporous-coated titanium at the density of 1 × 10⁴ cells/cm². After culturing for 12 h, samples were fixed by glutaraldehyde and osmium, performing gradient dehydration by alcohol and replacement by isopentyl acetate. The surface was sprayed and dried at the critical point, and the adhesion and extension of the cells were observed by using scanning electron microscopy.

2.3. Antimicrobial Effect of Microporous Coatings Containing Zinc on Staphylococcus aureus. *Staphylococcus aureus*-lyophilized strain was cultured into solid culture medium, incubated in a 37°C incubator for 24 h, and transferred once for each day, to the third generation. The inoculating loop was used to scrape a little of the activated bacteria that was

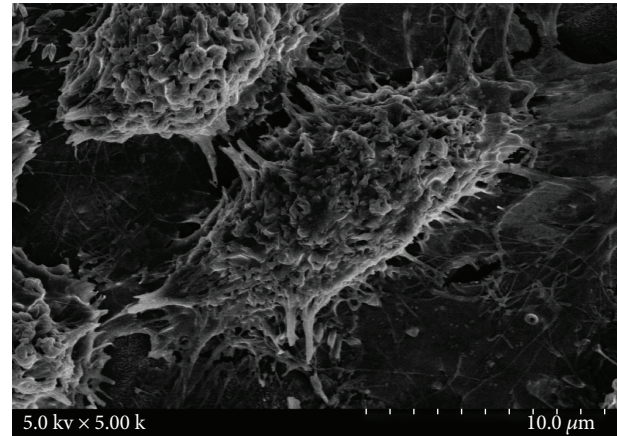


FIGURE 1: SEM of osteoblasts cultured on microporous coatings containing zinc titanium surface of 12 h cell morphology.

added into the nutrient broth medium, and the bacteria concentration of 1 × 10⁵ cfu/ml was adjusted for application.

The ethylene oxide sterilized microporous coatings containing zinc titanium (the experimental group) and pure titanium (the control group) were placed in a petri dish. 1000 μL of PBS was added to the culture dish and 100 μL of the above-prepared bacteria solution was added to the surface of the two abovementioned materials, and then, incubation was performed in a constant temperature incubator at 37°C for 24 hours.

80 μL of the bacterial solution was taken from the surface of the above two groups and uniformly added to the nutrient agar medium, gently applied evenly, and then placed in a 37°C incubator for 24 hours. After incubation for 24 h, the number of viable bacteria colonies on material surfaces of the above two groups was counted.

The antimicrobial ratio of the microporous coatings containing zinc material was calculated according to the following formula: $R = (\text{average number of colonies recovered in the blank control group} - \text{number of colonies recovered in the experimental group}) / \text{average number of colonies recovered in the blank control group} \times 100\%$.

3. Results

Figure 1 shows the morphology of osteoblasts cultured on the surface of microporous coatings containing zinc for 12 h. It clearly shows osteoblast eminentia on the surface of microporous coatings containing zinc, with large cell volume. The spreading of cells on the material surface is well, and osteoblasts tightly adhere to the surface of microporous coatings containing zinc through lamellipodia and filopodia, presenting obvious trend of the surrounding extension. The surface of cells is rough, with rich secretory granules, indicating that the osteoblasts have good adhesion and extension property on the surface of microporous coatings containing zinc.

The antimicrobial effect of the above two materials on *Staphylococcus aureus* is shown in Figure 2, where A and B present the bacterial colony plate count photos of pure titanium surface and microporous coatings containing zinc

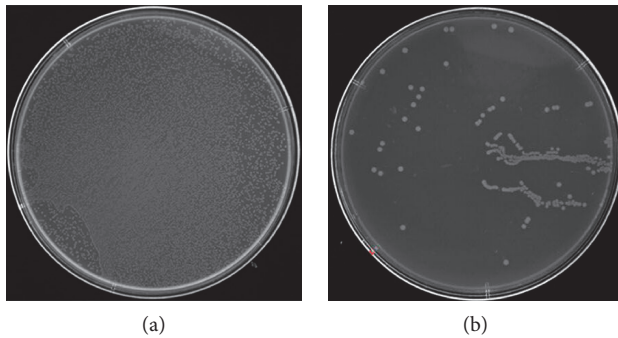


FIGURE 2: Colony count of *Staphylococcus aureus* on the sample surface after 24h culture. (a) Pure titanium and (b) microporous coatings containing zinc titanium surface.

titanium surface, respectively. We can see that in Figure 2(a), *Staphylococcus aureus* on the surface of pure titanium (control group) is densely covered with the entire culture dish. Figure 2(b) shows the bacterial colonies on the microporous coatings containing zinc titanium surface, and the number of *Staphylococcus aureus* colony is reduced greatly. The number of colonies is very few, indicating that the microporous coatings containing zinc on titanium surface can effectively inhibit the growth of *Staphylococcus aureus* colonies, with a good antibacterial effect.

4. Discussion

Adhesion of cells on the surface of the material is a prerequisite and the basis for the subsequent biological behavior of cells. The quality of cell adhesion on the surface of the material determines the subsequent biological behavior of the cells, including proliferation, differentiation, and apoptosis. But the adhesion of cells on the surface of the material is an extremely complex process, and the whole process is subject to the regulation of complex signal network process [8]. It has been found that the adhesion of cells to the surface of material undergoes a number of processes such as cellular attachment, extension, and focal connection. The whole process involves the regulation of many molecular proteins, which interact with each other, inducing cell signaling and then induce transcription factors. Studies have found the physical and chemical properties of cell surfaces such as surface morphology, roughness, chemical composition, hydrophilicity, and hydrophobicity [9], and the surface charge and surface free energy interact with and promote each other; for example, for materials with proper roughness, its surface hydrophilicity and surface energy are high, and it is easy to adsorb the protein in the body fluid, and through the interaction of its secretory adhesion receptors and synthetic adhesion proteins with surface adsorbent protein, the cells will ultimately adhere to the surface of the material closely.

Studies have shown that the surface roughness of the material can promote cell adhesion, and its mechanism may be that rough surface increases the wettability and hydrophilic properties of the surface of the material, and thus promote cell adhesion. Our findings are consistent with the

literature. Wu et al. [10] found that the hydrophilicity, surface roughness, and cell viability of MAO-processed material surface cells were significantly increased, which was helpful for the formation of apatite, improving the bioactivity of the titanium alloy surface, to promote the cell adhesion and proliferation. Liu et al. [11] found that the adhesion and proliferation of MAO-processed Ti-24Nb-4Zr-7.9Sn surface osteoblasts were significantly increased, with a good bioactivity and biocompatibility. Adhesion of cells was the basis of cell behavior and basis for cells to play a biological role, and it had an important impact on the subsequent cell proliferation, differentiation, mineralization, and apoptosis. In this study, we found that osteoblasts had a good adhesion in the microporous coatings containing zinc titanium surface, indicating that titanium-based metal surface microporous coatings containing zinc have a certain osteogenic performance on osteoblasts. We will further study the effect of this coating material on the proliferation, differentiation, mineralization, and apoptosis of osteoblasts in the future. And based on this, we will implement further study on the regulation of molecular mechanism of this coating material on osteoblasts to lay a good theoretical basis for clinical application.

Studies have shown that when titanium-based metals are implanted as implants, the bacteria and host cells will be competitive to reach the surface of the implants and competition results of bacteria and host cells directly affect the fate of the implants [12, 13]. If the bacteria adhere to the surface of the implants at first, it will quickly proliferate on the surface, and the result will inhibit adhesion and proliferation of osteoblasts in the implants' surface, resulting in infection. In contrast, if osteoblasts adhere to the surface of the implants at first, the bacteria will be inhibited from adhering to and proliferating on the surface. Studies have shown that the ability of anti-infection increases along with the increase of biological activity and biocompatibility of implanted materials, which may be closely related to competitive inhibition between bacteria and host cells. In view of the current view, we design to achieve excellent surface morphology, good biocompatibility, and biological activity of implants by surface modification, thereby reducing or inhibiting the occurrence of implant-related infections.

As an inorganic antibacterial agent, metal element has been widely used in clinical practice, such as the clinically used nanosilver application and sulfadiazine argentineum (SD-Ag) used in the burn department, which have all achieved good clinical efficacy. Zinc, as another important inorganic antimicrobial agent, has been proved to have a good antibacterial effect, but the specific mechanism is still unknown. It is believed that many factors may act together, involving bacterial synthetase, local microenvironment of bacteria, etc.

In the present study, we found that microporous coatings containing zinc titanium have good antibacterial effect, but the exact mechanism is not known and still awaits further exploration. The existing research shows that microporous coatings containing zinc can produce a lot of reactive oxygen species, especially hydrogen peroxide, which is a strong oxidizing agent that reduces bactericidal activity, finally leading to the reduction of adhered bacteria on the coating

surface. Further study reveals that when the zinc ions interact with the bacteria, zinc ions are firmly adsorbed on the cell membrane with the Coulomb force because the cell membrane is negatively charged and the zinc ion is positively charged and further penetrate the cell walls of bacteria. Subsequently, the zinc ions interact with protein, thiol (-SH), and amino (-NH₂) in nucleic acid, which cause bacterial protein denaturation, destruction of bacterial synthetase activity, lower environmental pH value, etc. Under the combined effects of these factors, ultimately, it will lead to the death of bacteria due to loss of proliferation capability. Our study results are consistent with the literature reported. Jin et al. [14] prepared the coatings containing zinc on the surface of titanium alloy by ion implantation technology, and in vitro studies show that it has antibacterial and osteogenic properties, with good application prospects. Reyes-Vidal et al. [15] prepare zinc/silver composite coating by electrodeposition, and results show that the composite coating had a good antibacterial effect. Compared with these preparation methods, the microporous coatings containing zinc prepared by MAO technology in this study combined strongly with the substrate, and more importantly, zinc was uniformly doped on the surface of the coating, achieving slow release when implanted in the body, so it has antibacterial and osteogenic properties, with a good application prospect.

The integration of surface structure and biomedical function of medical metal materials is a challenging and innovative idea in the field of metal implantation. It is also a hot and difficult point in the research of surface interface of metal implant materials. Using the appropriate release of human beneficial elements to achieve the biomedical function of a medical metal material is a valuable study with important clinical application values. Through the study of effects and antimicrobial properties of microporous coatings containing zinc on the biological behavior of osteoblasts, it aims to provide a new idea and method for promoting long-term and permanent biostability of implants, with an important theoretical significance and application prospect.

Conflicts of Interest

The authors declare that they have no conflicts of interest.

Acknowledgments

This study was supported by the Natural Science Foundation of Jiangsu Province (Grant No. BK20140123).

References

[1] E. P. Lautenschlager and P. Monaghan, "Titanium and titanium alloys as dental materials," *International Dental Journal*, vol. 43, pp. 245–253, 1993.

[2] Z. F. Yin, L. Wu, H. G. Yang, and Y. H. Su, "Recent progress in biomedical applications of titanium dioxide," *Physical Chemistry Chemical Physics*, vol. 15, p. 4844, 2013.

[3] Z. L. Shi, P. H. Chua, K. G. Neoh, E. T. Kang, and W. Wang, "Bioactive titanium implant surfaces with bacterial inhibition and osteoblast function enhancement properties," *The International Journal of Artificial Organs*, vol. 31, pp. 777–785, 2008.

[4] L. Le Guéhennec, A. Soueidan, and P. Layrolle, "Surface treatments of titanium dental implants for rapid osseointegration," *Dental Materials*, vol. 23, pp. 844–854, 2007.

[5] Y. Wang, H. Yu, C. Chen, and Z. Zhao, "Review of the biocompatibility of micro-arc oxidation coated titanium alloys," *Materials & Design*, vol. 85, pp. 640–652, 2015.

[6] J. Aaseth, G. Boivin, and O. Andersen, "Osteoporosis and trace elements—an overview," *Journal of Trace Elements in Medicine and Biology*, vol. 26, pp. 149–152, 2012.

[7] Q. M. Zhao, L. Cheng, Z. T. Liu, and J. J. Zhao, "Surface characteristics of Zinc-TiO₂ coatings prepared via micro-arc oxidation," *Composite Interfaces*, vol. 21, pp. 585–593, 2014.

[8] R. G. Triplett, U. Froberg, N. Sykaras, and R. D. Woody, "Implant materials, design, and surface topographies: their influence on osseointegration of dental implants," *Journal of Long-Term Effects of Medical Implants*, vol. 13, p. 18, 2003.

[9] L. Feller, R. Chandran, R. A. Khammissa, R. Meyerov, Y. Jadwat, and M. Bouckaert, "Osseointegration: biological events in relation to characteristics of the implant surface," *South African Dental Journal*, vol. 69, p. 114, 2014.

[10] J. Wu, Z. M. Liu, and X. H. Zhao, "Improved biological performance of microarc-oxidized low-modulus Ti-24Nb-4Zr-7.9Sn alloy," *Journal of Biomedical Materials Research Part B: Applied Biomaterials*, vol. 92, p. 298, 2010.

[11] Z. M. Liu, B. Gao, and L. Z. Zhang, "Experimental study of Ti-24Nb-4Zr-7.9Sn alloy after treated with micro-arc oxidation in vivo," *Hua xi kou qiang yi xue za zhi = Huaxi kou-qiang yixue zazhi = West China journal of stomatology*, vol. 26, p. 595, 2008.

[12] P. A. Norowski Jr. and J. D. Bumgardner, "Biomaterial and antibiotic strategies for peri-implantitis: a review," *Journal of Biomedical Materials Research Part B: Applied Biomaterials*, vol. 88, pp. 530–543, 2009.

[13] R. M. Donlan and J. W. Costerton, "Biofilms: survival mechanisms of clinically relevant microorganisms," *Clinical Microbiology Reviews*, vol. 15, pp. 167–193, 2002.

[14] G. Jin, H. Cao, and Y. Qiao, "Osteogenic activity and antibacterial effect of zinc ion implanted titanium," *Colloids and Surfaces B: Biointerfaces*, vol. 117, pp. 158–165, 2014.

[15] Y. Reyes-Vidal, R. Suarez-Rojas, and C. Ruiz, "Electrodeposition, characterization, and antibacterial activity of zinc/silver particle composite coatings," *Applied Surface Science*, vol. 342, pp. 34–41, 2015.

Review Article

Analysis of Drag Reduction Methods and Mechanisms of Turbulent

Gu Yunqing,^{1,2} Liu Tao,¹ Mu Jiegang,¹ Shi Zhengzan,¹ and Zhou Peijian¹

¹College of Mechanical Engineering, Zhejiang University of Technology, Hangzhou 310014, China

²School of Energy and Power Engineering, Jiangsu University, Jiangsu, Zhenjiang 212013, China

Correspondence should be addressed to Gu Yunqing; guyunqing@zjut.edu.cn

Received 30 April 2017; Accepted 20 August 2017; Published 18 September 2017

Academic Editor: Saurabh Das

Copyright © 2017 Gu Yunqing et al. This is an open access article distributed under the Creative Commons Attribution License, which permits unrestricted use, distribution, and reproduction in any medium, provided the original work is properly cited.

Turbulent flow is a difficult issue in fluid dynamics, the rules of which have not been totally revealed up to now. Fluid in turbulent state will result in a greater frictional force, which must consume great energy. Therefore, it is not only an important influence in saving energy and improving energy utilization rate but also an extensive application prospect in many fields, such as ship domain and aerospace. Firstly, bionic drag reduction technology is reviewed and is a hot research issue now, the drag reduction mechanism of body surface structure is analyzed, such as sharks, earthworms, and dolphins. Besides, we make a thorough study of drag reduction characteristics and mechanisms of microgrooved surface and compliant wall. Then, the relevant drag reduction technologies and mechanisms are discussed, focusing on the microbubbles, the vibrant flexible wall, the coating, the polymer drag reduction additives, superhydrophobic surface, jet surface, traveling wave surface drag reduction, and the composite drag reduction methods. Finally, applications and advancements of the drag reduction technology in turbulence are prospected.

1. Introduction

With the rapid increase of energy consumption, energy problem has been a global issue, which must be faced with and solved. Energy conservation and consumption reduction become an important research project at home and abroad. Drag reduction technology is urgently needed in transportation and military fields to reach the energy-saving goal. It is indicated by investigation and research that when the ship is sailing under water, the frictional force of its surface can account for 70% ~ 80% of total resistance. Even in the case of high-speed operation, its frictional force can also account for about 40% [1]. It can be calculated that in the case of certain power and energy, when the resistance decreases by 10%, the ship's speed and distance will increase by about 3.57% [2]. When the Reynolds of fluid in a round pipe reaches 10^5 and the turbulence intensity is 10%, Reynolds turbulent stress will be about 100 times as much as laminar viscous stress and the greater the stress is, the greater the loss of energy is, there will be a lot of energy consuming in the flow friction [3]. In a

sense, lot of energy consumption will be saved every year, even by slightly reducing the sailing resistance under water, which is of great significance for easing the energy crisis in the case of relative energy shortages nowadays.

Based on this, people always devote themselves to researching drag reduction methods. Natural creatures form a series of biological structure adapting to drag reduction after years of evolution. In recent years, scientists have found that the surface structures of many creatures are nonsmooth, the skins of sharks and dolphins have distributed many flake-like rib structures [4], which can change the skin's surface structure of turbulent layer and velocity distribution when the shark is swimming [5], while the earthworm's back can secrete some milk-white liquids, thus having wetting function and being able to reduce soil adhesion to the animal's body surface, which can research the goal of drag reduction [6]. These conditions of drag reduction on natural creatures give us great insights. Additionally, people also reach and develop many drag reduction methods, which provide many kinds of ways and means, attaining a series of achievements.

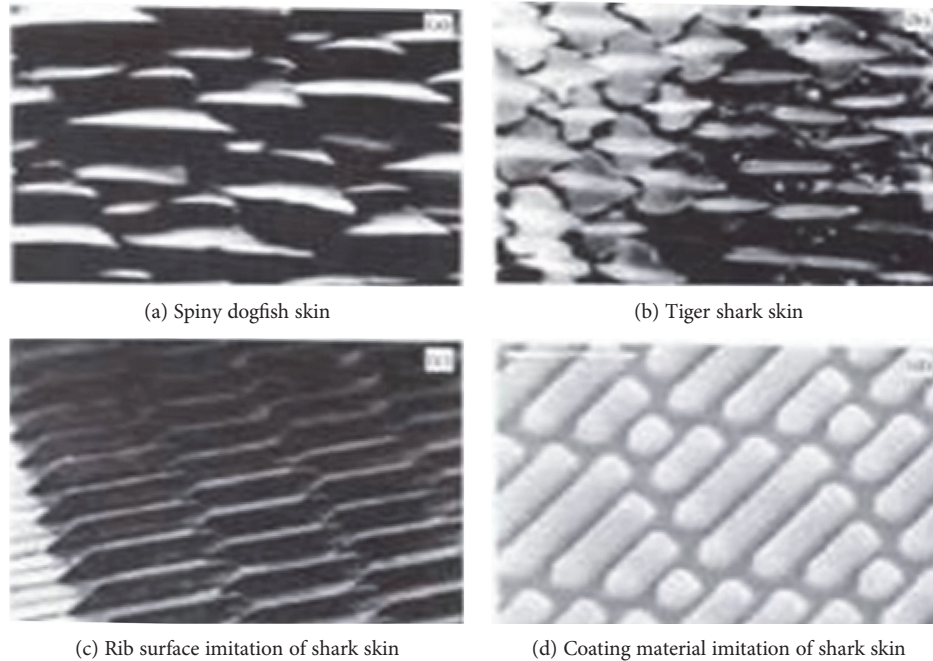


FIGURE 1: Shark skin microstructure and its imitation.

2. Bionic Drag Reduction Technology

2.1. Bionics. Bionics is an emerging discipline which can produce bionic productions, approximately with some characteristics of biological surfaces by imitating biological systems or using artificial technology to design and optimize productions for the biological function itself and to process for many aspects in function, shape, structure, material, and so on [7]. Natural creatures have developed into many kinds of biological bodies adapting to the environment in order to meet the need of living. These structures, shapes, and other relevant factors form the maximal ability to adapt to and coordinate the living environment by optimizing and coupling [8, 9]. Bionics was first born in the West in 1960. At an early stage, people understood and imitated natural creatures to apply this in practical production and life. As early as 2000 years ago in China, people began to imitate natural creatures consciously, for example, the famous carpenter in ancient times, Lu ban, invented saw for lumbering by observing the jagged edges of blades grass. In today's world, bionics has undergone rapid development, some research achievements have applied in people's daily life, for example, ultrasonic testing was invented by researching the bat [10], and riblet surface drag reduction was proposed by observing the shark when swimming [11].

2.2. Biological Surface Structures

2.2.1. Shark Skin's Nonsmooth Surface. The shark is one of the fastest swimming animals in the ocean, whose skin surface does not adhere to any halobios, having an excellent drag reduction effect. By long-term observation for shark-skin, its surface is not smooth but is composed of many scales with grooved shape, with more spines and setae [12].

Sharkskin's microstructure and its mimic are shown in Figure 1 [13]. The scales of sharkskin are shield scales, whose configuration are compact, orderly, and jagged. The middle teeth are long, while the side teeth are short. The tooth spaces are toward the shark's tail direction and have overlapping phenomenon. Lot of researches reveal that the special structure of sharkskin mainly has two aspects of the role: on the one hand, this structure has antifouling function, decreasing adhesion on skin by other benthos; on the other hand, it is in favor of drag reduction in swimming. The cause of drag reduction is that this structure can change the intrinsic structure and the velocity distribution in turbulent boundary layer when the shark is swimming, which has a good effect on drag reduction.

2.2.2. Earthworm's Nonsmooth Skin. The earthworm is a kind of soft animal, which has the characteristic of reducing adhesion to move freely without soil adhesion in clay soil. Through the biomechanical angle of earthworm crawling, the frictional resistance between the body and the soil surface was analyzed. The characteristic of an earthworm is the result of coupling with many factors, for example, earthworm's nonsmooth skin, its soft figure, and special way of movement [14, 15]. Earthworm's skin structure is shown in Figure 2 [6]. The back hole of the earthworm is concave pit on a nonsmooth surface structure. It can secrete some milk-white liquids and wet the surroundings, which can form a lubricated interface between soil and earthworm's body, reducing the adhesion of soil for the creature's skin.

2.2.3. Dolphin's Flexible Body Surface. The mystery of high-speed and low resistance, when the dolphin is swimming, is always one of the hot research issues for all countries'

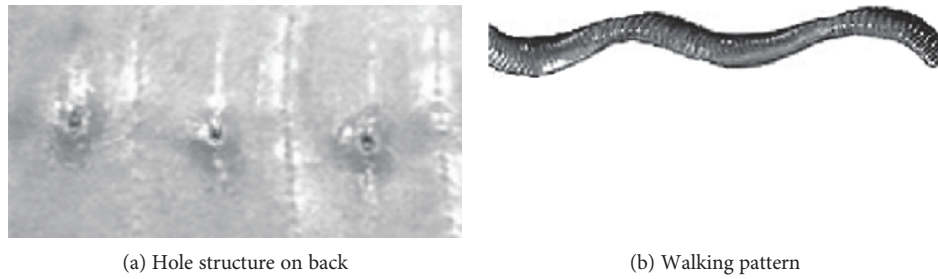


FIGURE 2: Earthworm's body surface.

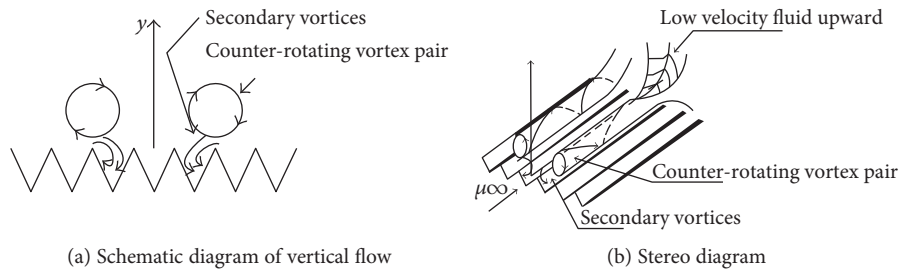


FIGURE 3: Schematic diagram of the interaction between the grooved surface and streamwise vortex.

scientists. The United States, Europe, and other countries have conducted plenty of theoretical studies and experimental researches, currently attempting to find the drag reduction mechanism of the dolphin's skin, which is mainly composed of two parts by research: for one thing, in the process of dolphin's swimming, its eyes can secrete a special liquid, which covers the whole skin coordinating with the streamline body shape curve of the dolphin. The liquid can reduce the friction force when the dolphin is swimming, having a lubricating function; another most key cause is that the dolphin can produce a wave in the process of swimming. It is produced from the dolphin's head, transferring to the tail at a very high frequency and minimum amplitude, changing the dolphin's skin into a flexible skin, which is very similar with the mechanism of flexible wall drag reduction. What is more, the dolphin's skin wave can produce vortex layer when the dolphin is swimming, which has an effect on drag reduction to some extent [16].

2.3. Bionic Drag Reduction Methods

2.3.1. Groove Surface Drag Reduction. In the field of traditional thought, people always focus more energy on the smooth surface drag reduction. With the further research of bionics, people find that the microgrooved surface can effectively reduce the frictional force on the wall. At present, the practical applications of groove surface drag reduction mainly focus on 3 parts: aircraft, fluid drive apparatus, and pipeline fluid conveying equipment [17]. As early as the 1980s, German aircraft manufacturers began to use this technology. They found that through the technology, 8% of the fuel could save, when the plane flew the same distance. Currently, the United States, Europe, and other countries study deeply the groove surface drag reduction when the aircraft is flying and achieves great development.

By researching the groove surface drag reduction, there are mainly two aspects that influence its characteristic: its characteristic and the flow-field environment. The self-factor of groove surface includes its shape and size. The flow-field environment includes its pressure gradient, the shape of flow cross-section, and the fluid velocity. Researching a variety of geometries of groove (including V-shape, oval, semicircular, jug, and rectangular), the drag reduction effect of the V-shape groove is the best [18]. In the study of the placement of groove surface, the surface in distribution of the flow direction can effectively control the quantity of the low strip, while the distribution of lateral direction can inhibit the length of the low strip. There is a big difference between researchers about the influence of placement mode on resistance, and the result of experiment still has a big discrepancy.

The optimal drag reduction surface is not the smooth surface as is described by classic experiments [17]. Groove surface drag reduction is related to the turbulent flowing structure. We can make a summary as follows by researching its mechanism at present; considering wall shear stress simply from fluid mechanics perspective, the groove surface drag reduction mechanism owes to the increase of the viscous sublayer thickness. The surface has an obvious delay in the transition from laminar boundary layer to turbulent boundary layer [19], which can also change the turbulent characteristics in the near wall region [20–22]. From the theory of turbulent coherent structure, its mechanism is that the streamwise vortexes associated with low-speed strips are reduced and the spanwise gather of the low-speed strips is suppressed under the interaction between streamwise vortexes and secondary eddies, as shown in Figure 3, which is produced under the groove. The strip transition on the groove surface is more flat compared with the smooth surface. Low-speed strip transitions have a good linearity, revealing that the groove restrains the lateral

fluid flow and strengthens the stability of fluid flow. From the principle of mechanical drag reduction, a similar “air bearing theory” can be put forward.

2.3.2. Flexible Wall Drag Reduction. After a long-term study of dolphins and sharks, people find these marine organisms’ skins are heavily elastic, which can reduce drag while they are swimming. According to this characteristic, scientists invent the flexible wall drag reduction method, daubing polymers on the solid wall and filling in their space with liquid to buffer external pressure with high elasticity. Both Cooper and Carpenter devote themselves to optimizing compliant coating to attain the best effect on drag reduction [22]. Russian scholars, Kulick and Semonov prove that the flexible wall has an important influence in reducing flow noise and surface frictional force by researching, the biggest drop up to 7%.

The flexible wall drag reduction mechanism is mostly increasing the thickness of the wall viscous sublayer, putting off the transition from laminar boundary layer to turbulent boundary layer and reducing the velocity gradient on the boundary layer, which results in reducing the shear force on the solid wall [23]. Even though, it still has a certain limitation, which is applicable to the high-speed and turbulent state. Its witnesses are exposed in low-speed flowing. Applying the flexible wall in the low-speed flow, it can reduce its own weight and deepen the depth of ship into the water. In this condition, its effect on drag reduction is not ideal.

3. Other Drag Reaction Methods

3.1. Microbubble Drag Reduction. Microbubble drag reduction is one of the main approaches in achieving jet drag reduction. With the depth of microair bubble drag reduction, it mainly applies in many fields, such as ship drag reduction, ultrasonic imaging, and sewage disposal. It is worth mentioning that microbubbles have an increasing effect on ship drag reduction, which becomes one of hot research issues. For a sailing ship, drag reduction can be achieved by covering the bubble layer on the hull. Reducing the density of the fluid medium with this method can change the boundary internal structure and the flowing kinematic and dynamic characteristics of the fluid in the near wall region, as shown in Figure 4. Meanwhile, we can take advantage of the small frictional force on the bubble surface and deformable regulating flow structure to reduce drag [24, 25]. Studies have shown that the drag reduction efficiency is up to 20% ~ 80%. Its mechanism is very complicated and affected by many factors, such as the number of hull surface, the size of bubbles, the structure of the hull, and flow parameter on the hull surface, which can affect the drag reduction effect [24]. For the hull surface, a gas-liquid mixture can be formed by injecting air, which can change the internal structure. Because of the volatility of the bubbles, partial work, produced by applying the shear force in the fluid, translates into deformation energy, reducing the loss of energy to the drag reduction effect.

Presently, about the study of micro bubbles, the foreign scholar, Madavan et al., [26] researches the factors of influence in the microbubble drag reduction. Merkle researches the microbubble turbulent boundary layer effect of plat.



FIGURE 4: Bubble reduction ship.



FIGURE 5: Supercavitating missile.

The study relatively lags behind and starts late in our country. Based on the achievements of his predecessors, Wang [27] researches the theory of microbubble drag reduction mechanism using the Mac method axisymmetric body in computational fluid dynamics. Now, using the technology in the field of super gun shells can reduce the resistance, thereby increasing the speed of water missile as shown in Figure 5.

Similar with flexible wall drag reduction, though microbubble drag reduction has obtained a substantial progress, it also has many weaknesses. An obvious weakness is that the bubbles covering the hull surface are not steady and vulnerable to cracks to generate enlarged drag force and noise. If the bubbles are too small, the needed drag reduction cannot be achieved [24]. Besides, its another weakness is that when the ship is sailing, the microbubbles covering on its surface are mainly hydrogen and oxygen bubbles generated by electrolyzing water. Though the source of reactant is abundant and its resultants are not polluttional to the environment, the degree of demand for and dependence on electric energy is very high.

3.2. Vibrant Wall Drag Reduction. Relative to the previous several drag reduction method, wall vibration reduction is a relatively new drag reduction technology, which refers to the exhibition along the flow direction of the fluid flow through the smooth plate and vibration, which leads to a method of flat surface resistance decreased, as shown in Figure 6. Jung et al. verified the effectiveness of drag reduction about periodic spanwise vibration of smooth flat plate in 1992, using DNS means for the first time [28]. In recent years, foreign scholars have revealed the vibrant wall drag reduction mechanism by adopting DNS computational method and analyzing DNS data. There are two drag reduction mechanisms about the vibrant wall at present: first, the

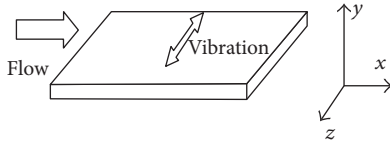


FIGURE 6: Schematic diagram of spanwise wall oscillation.

strips and vortices generate an obvious incline, which can produce negative spanwise vortices decreasing the mean velocity gradient in viscous sublayer and influencing the structure of the turbulent boundary layer. The streamwise vortices rearrange along the spanwise, weakening the wave intensity of the streamwise vortices in the lateral boundary layer, which is in favor of drag reduction. Another theory is that wall vibration interferes with the regenerative cycle of the quasi-streamwise vortices, not sustaining wall turbulence, which can achieve the effect of drag reduction [22]. Because of the complexity of turbulence, there is no accurate expression about wall drag reduction at present and relevant researches need to be done in the future.

3.3. Coating Drag Reduction. With the rapid development of the economy, the demand for crude oil is increasing. Pipeline construction is imminent. In the long distance transportation of oil process, the friction drag between the oil and pipeline accounts for 98% of the total drag, which makes the power of the pump station almost entirely overcomes friction [29]. If the transportation drag of oil can be reduced, it can bring huge economic benefits. Based on this, the drag reduction problem in the pipeline has always puzzled researchers. With the development of coatings technology, coating in the pipeline as a mature technology has been applied in the long distance transportation of oil. The application of the coating in the pipeline can not only reduce the resistance, but also reduce the corrosion of the oil pipeline. As early as 1953, this method was applied in gas transportation in trunk pipeline of oil, which can increase the gas transportation capacity by 5% ~ 20% [30]. Wei and Ni discover the drag reduction effect of silicone oil is the best. The reason is the hydrophobicity of silicone oil can make the wall more smooth [29]. The hydrophobicity of coating and control for wall roughness is the essential reason of coating drag reduction.

The coating drag reduction mechanism mainly focuses on two aspects: smooth surface drag reduction and low surface energy drag reduction. In the pipeline process, because of the limitation of working accuracy, the pipeline always presents a certain degree of roughness and its surface is rugged. The flowing of oil in the pipeline is in turbulent state, which can form vortex area on the surfaces of concave-convex objects which can generate a certain pressure, bringing loss of energy which is related to the mean height of concave-convex objects. The higher the mean height is, the greater the loss of energy is. The coating on the tube wall can effectively smooth the wall to reduce the concave-convex height, which can reduce the mechanical drag produced by wall roughness. It is discovered by foreign relevant researches that the transition from laminar boundary layer to turbulent boundary layer can be put off by spraying

compliant coating. For the low surface energy drag reduction, spraying compliant coating changes the wetting degree of the fluid on the tube wall because of the hydrophobicity of coating, reduces the velocity gradient of the fluid on the tube wall and, decreases the shear force on the wall, which can reach the goal of reducing the transportation drag. What is more, the difficulty that coating can be wetted is related to its drag reduction performance. The more difficult the coating can be wetted, the worse its drag reduction effect is.

3.4. Polymer Additive Drag Reduction. Besides the coating drag reduction, the drag reduction purpose also can be achieved by adding the polymer in the fluid. In the late 19th century, people found that muddy water can flow faster than clean water in some river sections. Later, they found that the frictional drag on the ship's surface is smaller when its sails in the water with water plants than without water plants [31]. In the late 1940s, Toms found the earliest drag reduction agent (DRA), polymethyl methacrylate (PMMA). Afterwards, researchers found other additives one after another. The DRA can be broadly divided into two categories: water-soluble and oil-soluble. Water-soluble DRA includes sesbania power, PAM (polyacrylamide), and synthetic PEO (Polyoxyethylene). Oil-soluble DRA includes olefin copolymer and polyisobutene [32].

In our country, though the study of DRA starts relatively late, great progress has still been made. In the 1980s and early 90s, Chengdu University of Science and Technology and Zhejiang University made a remarkable advance for the synthesis of indoor DRAs. The China Petroleum Pipeline Company made a breakthrough progress for the development of EP series oils, DRA, forming the independent intellectual property rights and starting mass production.

The polymer additives drag reduction is not still mature, but certain research results have been made. In 1967, Virk et al. discovered that there exists an elastic buffer area between laminar flow and turbulent flow in the near wall area, by measuring the fluid velocity before and after adding DRA, according to which, asymptote was being obtained. Early researchers consider that the existence of the elastic buffer area results in the enlargement of velocity and increase of flow in the pipe, attaining the drag reduction effect. Besides, Berman had a new discovery that the effect is better by injecting DRA than DRA is dissolved in liquid beforehand in 1986. Focusing on the influence of fluid kinetic characteristic, the polymer can change the turbulent structure on the wall. Abernathy drew two conclusions one is that polymer can impede the generation of eddies and reduce the frequency of vortex; the other is that polymer can reduce the rotation rate of the vortex. Both of them together can result in the drag reduction effect. Some hypotheses and analyses can be proposed combining with the experimental results for the polymer drag reduction mechanism, but there is still no unified theory which can explain all experimental phenomena [33, 34].

At the same time, artificial polymer can cause biological damage to the ship's hull, and some organic DRA can pollute the environment. So, the polymer drag reduction agent is commonly used for oil pipeline transportation, but it will add additional funding.

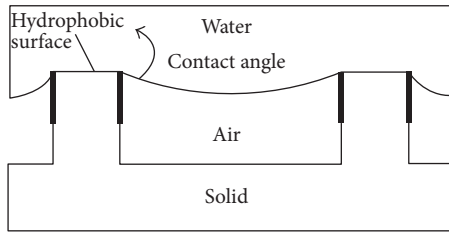


FIGURE 7: Schematic diagram of drag reduction mechanism of the superhydrophobic surface.

3.5. Superhydrophobic Surface Drag Reduction. According to the phenomenon, water rolls easily without wetting on the lotus leaf because of the microscale structure of the emulsion on the lotus leaf rejecting the water, it invented the method of the superhydrophobic surface drag reduction [35]. So far, the mechanism accepted of the superhydrophobic surface drag reduction is the theory of slip length considering that because water produces the wall slip through hydrophobic surface decreasing velocity gradient of the boundary layer, decreasing the shear stress, and delaying the change of laminar attachment surface, the laminar flow regime tends to be more stable [36]. The mechanism of the superhydrophobic surface drag reduction is shown in Figure 7.

Voronov et al. [37] found that by numerical simulation, while the slip length and contact angle are usually regarded as hydrophobic performance standards, they do not always follow the same rules, low σ_r (relative atomic size) tends to make the contact while the angle increases but will reduce the slip length. Bixler and Bhushan [38] obtained a maximum drag reduction rate of 26% by simulating shark skin resistance reduction experiments. Lee and Kim [39] had studied the applicable range of superhydrophobic drag reduction on hydraulic pressure. The present study found that the texture of the superhydrophobic surface captures the air to form the air cushion and reduces the frictional resistance between the fluid and the coating surface. Using the drag reduction characteristics of the superhydrophobic surface, the technique is applied to the surface of the swimming suit. As shown in Figure 8, this swimsuit is more conducive to increasing the speed of far mobilization compared to the imitation shark skin swimsuit.

3.6. Jet Surface Drag Reduction. The aim of jet technology is to control and provide power for itself through the interaction force of jet reaction and the interaction between jet and flow. It has short response time and good low voltage control characteristics [40].

Sharks living in the sea are aquatic animals having rapid movement. The burst start speed of the deep-sea sharks is amazing, reaching up to 10~20 m/s; while pursuing their prey, they have very fast speed [41]. There are large gill plates lined in front the body side of sharks, as shown in Figure 9, and each lamella has about 5~7 branchial cleft. As they swim, the water is sucked through the half opening mouth, and gas is exchanged from the gill slits. It is closely related with breathing and self-motion resistance reduction.

The researchers found the drag reduction effect on the surface of the jet according to the jet motion of the shark's gills. The present study generally believes that if there is jet on the motion face, jet fluid will block the mainstream field, forming the countercurrent area at the back of the jet hole and the direction of speed near the wall is contrary to flow velocity in the countercurrent area having the obvious drag reduction effect. Furthermore, there is the counter-rotating vortex extending downstream produced in the downstream of the jet hole and it would induce two vortex on the wall increasing the thickness of the boundary layer and decreasing the velocity gradient both having the effect of drag reduction [42].

To sum up, with the rapid development of science and technology, jet drag reduction technology has reached rapid development and fruitful achievements, many research results have been applied in the engineering practice, but there are still many problems that still need further research.

3.7. Traveling Wave Surface Drag Reduction. Traveling wave surface drag reduction technology is considered a very promising drag reduction technology and is made of corrugated shape, which was inspired from the undulating dunes structure of desert, as shown in Figure 10. At present, the mechanism of drag reduction for traveling wave surface is still controversial. A more persuasive argument is that the ripples on the surface of the traveling wave shape can produce secondary flow, namely the origin parallel artificial vortex flow sparked a row, so that it is free to flow in the parallel artificial vortex flow, achieving the goal of drag and noise reduction. Its principle is shown in Figure 11.

3.8. Combined Drag Reduction. In practical engineering application, multiple drag reduction technologies would be used together achieving the best drag reduction effect. The effect of drag reduction using multiple drag reduction technologies is generally better than that using single drag reduction technique. It is the most universal using trench surface drag reduction and other drag reduction methods together in a variety of combinations. A series of turbulent drag reduction tests on coupling of trench surface and polymer coating technology have been carried out turning out that the effect of coupled drag reduction is excellent for the trench surface drag reduction and polymer coating drag reduction. Sun and found that this combination increases the stability of the wall air layer can make bubble not easy to break reducing the resistance and noise, so that the effect of drag reduction is optimized [11].

4. Summary and Outlook

The turbulent drag reduction technique a case turbulence theory applied to engineering has good development prospects. Due to the need of practical engineering, Chinese and foreigners have carried out a large number of experimental studies and gotten many achievements as references for practical application. However, most studies still stay in the simulation and test phase having not forming the mature systemic theory. In future research, the exploration of drag

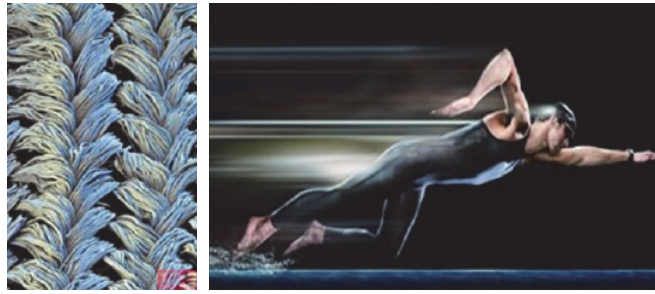


FIGURE 8: Bionic swimsuit.



FIGURE 9: Feature of shark gills.



FIGURE 10: Wavy structures in the desert.

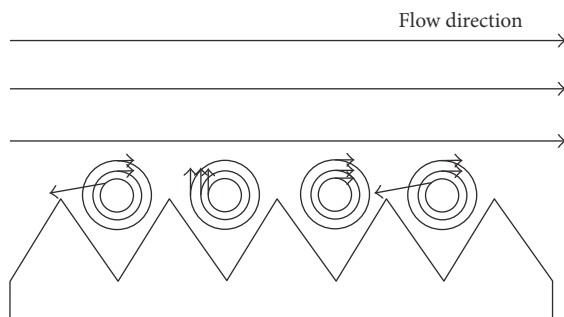


FIGURE 11: Schematic diagram of traveling wave.

reduction mechanism should be put into more important place, especially by combining the numerical simulation and experimental study and focus on theoretical research guiding practice with theory. The drag reduction effect is greatly restricted, due to that, the research work of the current technology of drag reduction is mainly focused on single

drag reduction technology. Therefore, to use multiple drag reduction technologies together will be an important direction for the future research. The research of technology is service for practice, so we should speed up the progress of promoting laboratory research results to the engineering application. And how to put the relatively mature drag reduction technology into actual projects and to promote it is also an important direction in the future research.

Conflicts of Interest

The authors declare that they have no conflicts of interest.

Acknowledgments

This project is supported by the National Natural Science Foundation of China (51779226, 51476144), the Zhejiang Provincial Natural Science Foundation of China (LQ15E050005), the Public Welfare Technology Application Projects of Zhejiang Province (2017C31025), and the China Postdoctoral Science Foundation (2016M601736).

References

- [1] Y. B. Li, Y. Q. Gu, J. G. Mou, S. H. Zheng, and L. F. Jiang, "Current research status of biomimetic drag-reducing antifouling paints with low surface energy," *Materials Protection*, vol. 47, no. 6, pp. 48–51, 2014.
- [2] J. L. Xu, X. R. Lai, B. Wang, L. Xu, and G. H. Liu, "Flow patterns and parameters of micro bubble generation in a flow focusing device," *Nanotechnology and Precision Engineering*, vol. 10, no. 1, pp. 59–63, 2012.
- [3] J. F. Sun, Y. Zhou, J. Li, X. S. Liu, and J. Y. Lan, "The design of testing equipment for drag resistance effect based on differential principle and the study of drag reduction characteristic of coatings," *Lubrication Engineering*, vol. 7, pp. 120–122, 2006.
- [4] Y. R. Sun and Z. D. Dai, "Bionics today and tomorrow," *Acta Biophysica Sinica*, vol. 23, no. 2, pp. 109–114, 2007.
- [5] Z. Y. Zhao and S. P. Dong, "Application of micro-grooved surface for turbulent drag reduction," *Journal of Petrochemical Universities*, vol. 17, no. 3, pp. 76–79, 2004.
- [6] Y. Q. Gu, J. G. Mou, D. S. Dai et al., "Characteristics on drag reduction of bionic jet surface based on earthworm's back orifice jet," *Acta Physica Sinica*, vol. 64, no. 2, article 024701, 2015.
- [7] Y. X. Lu, "Significance and progress of bionics," *Journal of Bionic Engineering*, vol. 1, no. 1, pp. 1–3, 2004.

- [8] H. Y. Wang, G. W. He, M. F. Xia, F. J. Ke, and Y. L. Bai, "Multi-scale coupling in complex mechanical systems," *Chemical Engineering Science*, vol. 59, no. 8-9, pp. 1677-1686, 2004.
- [9] E. T. Liu, "Systems biology, integrative biology, predictive biology," *Cell*, vol. 121, no. 4, pp. 505-506, 2005.
- [10] G. Neuweiler and E. Covey, *The Biology of Bats*, Oxford University Press, Oxford, 2000.
- [11] J. R. Sun and Z. D. Dai, "Bionics of non-smooth surface I," *Progress in Natural Science*, vol. 18, no. 3, pp. 241-246, 2008.
- [12] P. Ball, "Engineering shark skin and other solutions," *Nature*, vol. 400, no. 6744, pp. 507-509, 1999.
- [13] J. R. Sun and Z. D. Dai, "Bionics of non-smooth surface II," *Progress in Natural Science*, vol. 18, no. 7, pp. 727-733, 2008.
- [14] T. Shelley, "Worms show way to efficiently move," *Eureka*, vol. 24, no. 1, pp. 28-29, 2004.
- [15] L. Q. Ren, J. Tong, J. Q. Li, and B. C. Chen, "Soil adhesion and biomimetics of soil-engaging components: a review," *Journal of Agricultural Engineering Research*, vol. 79, no. 3, pp. 239-263, 2001.
- [16] F. E. Fish, "The myth and reality of Gray's paradox: implication of dolphin drag reduction for technology," *Bioinspiration & Biomimetics*, vol. 1, no. 2, pp. R17-R25, 2006.
- [17] D. B. Huang, X. H. Deng, and Y. J. Wang, "Numerical simulation study of turbulent drag reduction over riblet surfaces of tubes," *Journal of Hydrodynamics, Series A*, vol. 20, no. 1, pp. 101-105, 2005.
- [18] K. S. Chio, "European drag-reduction research—recent developments and current status," *Fluid Dynamics Research*, vol. 26, no. 5, pp. 325-330, 2000.
- [19] J. J. Wang, S. L. Lan, and F. Y. Miao, "Drag-reduction characteristics of turbulent boundary layer flow over riblets surfaces," *Shipbuilding of China*, vol. 42, no. 4, pp. 1-5, 2001.
- [20] H. W. Yang and G. Gao, "Experimental study for turbulent drag reduction using a novel boundary control technique," *Acta Aeronautica Et Astronautica Sinica*, vol. 18, no. 4, pp. 455-457, 1997.
- [21] Y. B. Li, Z. D. Qiao, and Z. Q. Wang, "An experimental research of drag reduction using riblets for the Y-7 airplane," *Aerodynamic Experiment and Measurement & Control*, vol. 9, no. 3, pp. 21-26, 1995.
- [22] A. J. Cooper and P. W. Carpenter, "The stability of rotating-disc boundary-layer flow over a compliant wall. Part 2. Absolute instability," *Journal of Fluid Mechanics*, vol. 350, pp. 261-270, 1997.
- [23] Y. Yao, C. J. Lu, T. Si, and K. Zhu, "Water tunnel experimental investigation on the drag reduction characteristics of the traveling wavy wall," *Journal of Hydrodynamics, Series B*, vol. 23, no. 1, pp. 65-70, 2011.
- [24] F. Guo, W. C. Dong, and Y. Bi, "The theoretical study on influencing factors to resistance reduction of a gyroidal object by microbubbles," *Journal of Harbin Engineering University*, vol. 31, no. 11, pp. 1443-1449, 2010.
- [25] K. Mohanarangam, S. C. P. Cheung, J. Y. Tu, and L. Chen, "Numerical simulation of micro-bubble drag reduction using population balance model," *Ocean Engineering*, vol. 36, no. 11, pp. 863-872, 2009.
- [26] N. K. Madavan, S. Deutsch, and C. L. Merkle, "Reduction of turbulent skin friction by microbubbles," *Physics of Fluids*, vol. 27, no. 2, pp. 356-363, 1984.
- [27] J. Q. Wang, *Elementary Study on Wall Skin Friction Reduction of Symmetrical Body by Microbubbles in Boundary Layer of Fluid*, Tianjin University, Tianjin, 2004.
- [28] A. Baron and M. Quadrio, "Turbulent drag reduction by spanwise wall oscillations," *Applied Scientific Research*, vol. 55, pp. 311-326, 1996.
- [29] J. T. Wei and B. Ni, "The drag reduction research of the additives in the heating network," *Journal of Changchun Institute of Technology*, vol. 12, no. 3, pp. 48-51, 2011.
- [30] D. W. Bechert, M. Bruse, W. V. Hage, J. T. Van der Hoeven, and G. Hoppe, "Experiments on drag-reducing surfaces and their optimization with an adjustable geometry," *Journal of Fluid Mechanics*, vol. 338, no. 5, pp. 59-87, 1997.
- [31] Y. R. Qun and Q. Si, "Study on heat transfer and drag reduction in flow boiling of polymer additives," *Chemical Engineering*, vol. 29, no. 5, pp. 22-25, 2001.
- [32] H. L. Petrie, S. Deutsch, T. A. Brungart, and A. A. Fontain, "Polymer drag reduction with surface roughness in flat-plate turbulent boundary layer flow," *Experiments in Fluids*, vol. 35, no. 1, pp. 8-23, 2003.
- [33] K. S. Choi, "Near-wall structure of a turbulent boundary layer with riblets," *Journal of Fluid Mechanics*, vol. 208, no. 6, pp. 417-458, 1989.
- [34] K. W. Li and Q. X. Lian, "A review on drag reduction of boundary layer," *Journal of Beijing University of Aeronautics and Astronautics*, vol. 4, pp. 68-76, 1991.
- [35] X. Q. Hao, L. Wang, Y. C. Ding, G. H. Ye, Z. Y. He, and B. H. Lu, "Study on the drag reduction of the superhydrophobic surface," *Lubrication Engineering*, vol. 34, no. 9, pp. 25-28, 2009.
- [36] X. L. Wang, Q. F. Di, R. L. Zhang, and C. Y. Gu, "Surface slip effect and its application to drag reduction technology," *Advances in Mechanics*, vol. 40, no. 3, pp. 241-249, 2010.
- [37] R. S. Voronov, D. V. Papavassiliou, and L. L. Lee, "Slip length and contact angle over hydrophobic surfaces," *Chemical Physics Letters*, vol. 441, no. 4-6, pp. 273-276, 2007.
- [38] G. D. Bixler and B. Bhushan, "Shark skin inspired low-drag microstructured surfaces in closed channel flow," *Journal of Colloid & Interface Science*, vol. 393, no. 1, p. 384, 2013.
- [39] C. Lee and C. J. Kim, "Underwater restoration and retention of gases on superhydrophobic surfaces for drag reduction," *Physical Review Letters*, vol. 106, no. 1, article 014502, 2011.
- [40] B. Srivastava, "Lateral jet control of a supersonic missile: computational and experimental comparisons," *Journal of Spacecraft & Rockets*, vol. 35, no. 2, pp. 140-146, 1998.
- [41] W. F. Reif, "Morphogenesis and function of the squamation in sharks," *Neues Jahrbuch für Geologie und Paläontologie, Abhandlungen*, vol. 164, pp. 172-183, 1982.
- [42] F. Li, G. Zhao, W. X. Liu, and Z. Z. Sun, "Simulation on flow control and drag reduction with bionic jet surface," *Journal of Basic Science and Engineering*, vol. 22, no. 3, pp. 574-583, 2014.